Alma Mater Studiorum · University of Bologna

Department of Physics and Astronomy "Augusto Righi"
Bachelor Degree in Physics

Dark matter spikes close to galactic black holes and their impact for DM signals at telescopes

Supervisor:
Prof. Filippo Sala

Submitted by:
Giovanni Dalena

Academic Year 2025/2026

Sommario

Lo studio della materia oscura è uno dei temi principali della fisica oltre il Modello Standard degli ultimi decenni. Ad oggi sono state raccolte numerose evidenze cosmologiche e astrofisiche indipendenti che richiedono la presenza di materia aggiuntiva non barionica, nota come materia oscura, la cui natura non è ancora stata determinata. Una delle principali tecniche per svelarne le interazioni non gravitazionali è la rivelazione indiretta, ossia l'uso di dati da telescopi per cercare segnali di annichilazione di materia oscura, previsti nei modelli in cui la materia oscura è una reliquia termica. L'obiettivo della tesi è studiare l'impatto delle incertezze relative al profilo di densità della materia oscura nella Via Lattea sui vincoli di rivelazione indiretta ottenuti dal Centro Galattico, il bersaglio più promettente per questo tipo di ricerca. Il numero atteso di eventi di segnale scala come il quadrato della densità di materia oscura, ed è quindi estremamente sensibile al profilo di densità assunto: per un insieme di profili rappresentativi, i cui parametri sono fissati tramite vincoli osservativi, il segnale previsto dalla regione centrale varia di oltre due ordini di grandezza da un profilo all'altro. Un semplice modello di reliquia termica è poi confrontato con i limiti sperimentali sulla sezione d'urto di annichilazione per valutarne la compatibilità. Nel Centro Galattico è inoltre presente il buco nero supermassiccio Sgr A*, la cui crescita adiabatica può ridistribuire la materia oscura circostante in una cuspide molto densa, detta spike, che può quindi migliorare drasticamente le prospettive di rivelazione indiretta. Ri-deriviamo quindi il profilo di densità della spike generato dalla crescita adiabatica di Sgr A* e ne valutiamo l'impatto sui vincoli, mostrando quanto fortemente essi dipendano dalla distribuzione più interna di materia oscura. Il codice sviluppato per questa tesi è disponibile pubblicamente all'indirizzo github.com/IvanDalena/Bachelor-thesis.

Abstract

The study of dark matter has been one of the main topics in physics beyond the Standard Model over the past decades. To date, several independent cosmological and astrophysical observations require the existence of additional non-baryonic matter, known as dark matter, whose nature has not yet been determined. A leading technique to uncover its non-gravitational interactions is indirect detection, i.e. the use of telescope data to look for signals of dark matter annihilations, which are predicted by the well-motivated thermal-relic dark matter models. The aim of this thesis is to study the impact of the uncertainties on the dark matter density profile of the Milky Way on the indirect detection constraints obtained from the Galactic Center, the most promising target for this kind of search. The expected number of signal events scales as the square of the dark matter density, and is therefore extremely sensitive to the assumed density profile: for a set of representative profiles, whose parameters are fixed through observational constraints, the predicted signal from the central region varies by more than two orders of magnitude from one profile to another. A simple thermal relic model is then compared with the experimental limits on the annihilation cross section to assess their compatibility. Moreover, the Galactic Center hosts the supermassive black hole Sgr A*, whose adiabatic growth can redistribute the surrounding dark matter into a very dense cusp, known as a spike, that can then dramatically enhance indirect detection prospects. We re-derive the spike density profile generated by the adiabatic growth of Sgr A* and assess its impact on the constraints, showing how strongly they depend on the innermost dark matter distribution. The code developed for this thesis is publicly available at github.com/IvanDalena/Bachelor-thesis.

Contents

Introduction

Objective and structure of the thesis

The objective of this thesis is to quantify how the astrophysical uncertainties on the dark matter (DM) density profile of the Milky Way affect the constraints obtained from indirect searches towards the Galactic Center. The gamma-ray flux expected from DM annihilation depends on the density profile through the J-factor, a line-of-sight integral of the squared density: as a consequence, different profiles lead to very different constraints. In order to show this, we compare a set of representative DM density profiles and confront their upper limits on the annihilation cross section with a simple thermal relic model.

The thesis is organized as follows:

- In the first chapter, we present the main properties of DM, together with its most relevant candidates: WIMPs. Then we discuss the most significant astrophysical evidence, on scales ranging from galaxies and galaxy clusters to the entire Universe. In addition, we briefly introduce theories of modified gravity, developed as an alternative to the DM hypothesis. Finally, we illustrate the theoretical framework for DM indirect searches and describe the main astrophysical environments investigated. The primary source for this chapter is *Dark Matter* [1], the most complete review on DM written to date.

- In the second chapter, we focus on the Galactic Center, the most promising target for DM indirect searches, unless the DM distribution exhibits a large core at its center. We introduce a set of representative DM density profiles and compute their J-factors. We then consider a simple model of thermal relic DM and constrain it with the upper limits on the annihilation cross section obtained by the H.E.S.S. Inner Galaxy Survey [2], assessing the impact of the density profile uncertainty on the constraints.

- In the third chapter, we study the adiabatic growth of the supermassive black hole at the center of our Galaxy, which redistributes the DM around it into a cusp, called a spike. Then we derive the relation between the slope of the spike and that of the DM halo and discuss it for different initial density profiles. We introduce two benchmark spike profiles, compute their J-factors and finally quantify the impact of the spike on the cross section limits derived in the previous chapter.

Finally, we summarize and discuss our main results and their implications.

All the code developed and used in this work for numerical calculations is available at github.com/IvanDalena/Bachelor-thesis.

Chapter 1

Dark matter

Evidence for the existence of DM comes from a wide range of astronomical scales: from a few kiloparsecs, corresponding to the typical size of a small galaxy, up to nearly the entire Universe.

In this chapter, after a concise description of the properties of DM and its leading candidates, we present this evidence over increasing scales: starting from the study of rotation curves of spiral galaxies, to the mass of galaxy clusters, with a brief mention of the Cosmic Microwave Background (CMB) and Large Scale Structures.

Since all this evidence can be explained through gravitational interactions, alternative theories of gravity have been developed: the most prominent one is Modified Newtonian Dynamics (MOND). However, none of these theories is currently able to explain all cosmological and astrophysical observations.

The present cosmological DM density, averaged over the total matter-energy content, is measured to be $\Omega_{\rm DM} = 0.264 \pm 0.003$ [1, 3]. Considering only the matter content, this value rises to about 84%. Figure 1.1 shows a comparison between the content of the Universe today and at the time of photon decoupling, the moment when photons decouple from matter and start to travel freely.

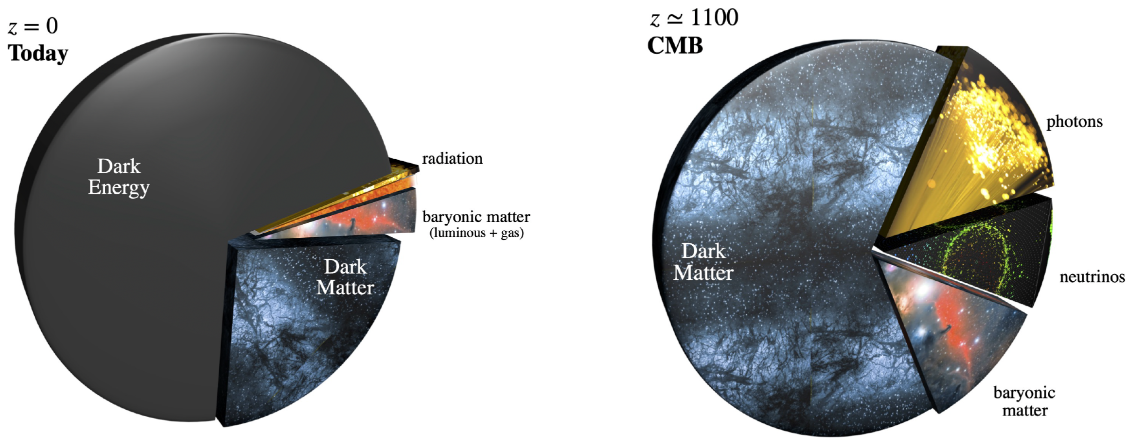

Figure 1.1: *Left panel: content of the Universe today. Right panel: content of the Universe at the time of photon decoupling. The different components evolve differently in cosmology [1, 3].*

1.1 Properties of dark matter and WIMPs

From astrophysical and cosmological observations it is possible to determine the general properties of DM: it turns out that it behaves as a kind of *cold, non-interacting, stable matter with adiabatic inhomogeneities*.

- **Matter** stresses the fact that DM behaves as matter in the cosmological evolution, i.e. its density decreases as the inverse of the volume.
- **Cold** means that DM behaves in large part as a non-relativistic fluid at the time of matter-radiation equality (MReq). Therefore, DM particles move slowly (with respect to the speed of light) and can attract each other and cluster. If they moved with velocities comparable to c, the clustering would not be effective and structures would not form and grow.
- **Non-interacting**, or equivalently **collision-less**, means that the interactions of DM with itself or between DM and ordinary matter are small enough to be neglected, except for gravitational interaction. For this reason it is called "dark matter": the absence of interactions with light makes DM *dark*.
- A consequence of the non-interacting nature is that DM is *dissipation-less*: unlike ordinary matter, it cannot emit electromagnetic radiation and therefore cannot easily dissipate its energy and cool down. This is the main reason why baryonic matter and DM behaved differently during cosmological evolution.
- **Stable** means that DM has been present since the early phases of the Universe, estimated to be $t_{\mathrm{Uni}} \simeq 13.8\,\mathrm{Gyr} = 4.35 \times 10^{17}\,\mathrm{s}$. Indirect detection constraints on DM decay indicate that its lifetime must be over 10 orders of magnitude longer than the age of the Universe.
- **Adiabatic** means that, on cosmological scales, its composition is the same everywhere. Moreover, DM and ordinary matter have the same primordial density inhomogeneities, indicating that the mechanism responsible for their generation is the same.

While there is broad consensus about the hypothesis that DM is made of one or more new particles beyond the Standard Model (SM) of particle physics, no definitive experimental confirmation has been obtained so far. Among the particles that satisfy these conditions, a well-motivated and widely studied class of candidates is given by the *Weakly Interacting Massive Particles* (WIMPs). WIMPs are assumed to interact through the weak force and gravity, with masses in the GeV-TeV range and a cross section characteristic of the electroweak scale, which justifies their name. It is assumed that in the early Universe WIMPs were in thermal equilibrium with the cosmic plasma, with an interaction rate Γ much larger than the Hubble expansion rate H. When $\Gamma \sim H$, they decoupled from the primordial plasma, the so-called *freeze-out*, breaking this equilibrium and fixing the average density of WIMPs in the Universe. The *WIMP miracle* consists in the fact that, by requiring this relic density to reproduce the observed DM abundance, one obtains an annihilation cross section [1] of order $\langle\sigma v\rangle \simeq 3 \times 10^{-26}$ cm^3/s, compatible

[1] Throughout this thesis we refer to $\langle\sigma v\rangle$ simply as the cross section, although strictly speaking it is the thermally-averaged cross section times relative velocity.

with electroweak-scale interactions. However, no conclusive signal, despite an extensive search program that combines, often in a complementary way, direct, indirect, and collider probes, has been detected so far. This situation might change in the near future with the advent of even larger detection experiments [4, 5]. For comprehensive reviews on the search for WIMPs see [6, 7].

1.2 Astrophysical evidence

1.2.1 Rotation curves of spiral galaxies

In 1970, Vera Rubin and Kent Ford initiated a true revolution in the field of DM after analyzing the rotation curves of the Andromeda Galaxy (M31) [8].

It is known that spiral galaxies rotate around their vertical axis, therefore we can infer their mass distribution from the rotation velocity, which can be measured experimentally through Doppler shift. From Newtonian mechanics we can derive the circular velocity $v_{\rm circ}$ of a body of mass m at a distance r from the center as a function of the mass M enclosed within r, assuming spherical symmetry

$$\frac{m\,v_{\rm circ}^2(r)}{r} = \frac{G\,m\,M(r)}{r^2} \quad \Rightarrow \quad v_{\rm circ}(r) = \sqrt{\frac{G\,M(r)}{r}}\,. \tag{1.1}$$

In spiral galaxies, most of the mass is concentrated relatively close to the center and along the disk arms. Therefore, beyond a certain radius r, $M(r)$ can be considered approximately constant and the circular velocity should follow a Keplerian decline $v_{\rm circ}(r) \propto r^{-1/2}$. The crucial point is that the observations of a large sample of galaxies of this kind have shown that the rotation curves instead remain *flat* out to large distances from the galactic centers. We show the results obtained by Rubin and Ford for the Andromeda galaxy in fig. 1.2.

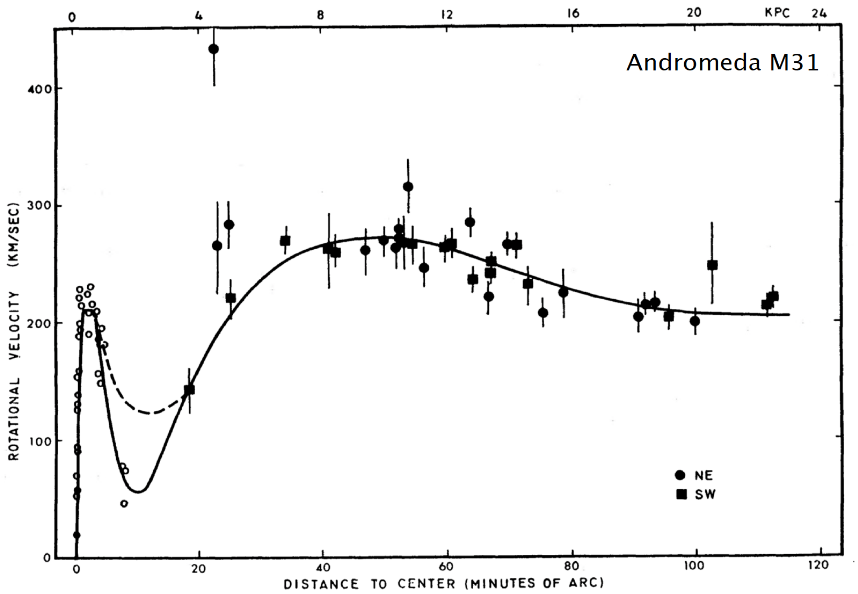

Figure 1.2: *Rotation curve of the Andromeda Galaxy (M31) as measured by Rubin and Ford [8]. Filled circles and squares distinguish the two halves of the major axis: NE and SW, while the open circles trace the innermost region. The solid line is the rotation curve, the dashed line is an alternative interpolation in the inner region, which is poorly sampled.*

To explain this discrepancy, additional invisible mass must be present to prevent the peripheral stars from flying away and the galaxies from breaking apart. Assuming spherical symmetry, eq. (1.1) shows that a constant velocity $v_{\mathrm{circ}}(r)$ is obtained assuming a matter *halo* that has mass density $\rho(r) \propto \frac{1}{r^2}$ out to large r: in this way, $M(r) = 4\pi \int_0^r dr'\, r'^2\, \rho(r') \propto r$ so that the dependence of $v_{\mathrm{circ}}(r)$ on r vanishes. Eventually, at even larger r, the halo is expected to die off and the rotation curve to start declining. However, no observable traces are typically available at such large distances [1].

To describe the DM distribution in more detail, numerical simulations are used: from N-body simulations, including only the DM component, one obtains a profile known as the Navarro-Frenk-White (NFW) [9, 10]

$$\rho_{\mathrm{NFW}}(r) \propto \frac{1}{\frac{r}{r_s}\left(1 + \frac{r}{r_s}\right)^2}, \tag{1.2}$$

where r_s is a characteristic parameter called scale radius [11].

1.2.2 Galaxy clusters

The first evidence of a mass-to-light discrepancy dates back to 1933, when Fritz Zwicky studied the velocity dispersion of several galaxy clusters and obtained unexpected results [12, 13]. Using the virial theorem, he estimated the mass of the clusters from the velocity dispersion of the galaxies, measured through Doppler shift, and found large discrepancies with the mass inferred from the observed luminous matter. Zwicky is also credited with introducing the term *dark matter*, although the concept itself had already been present in the scientific community for some years [14].

Particularly significant are the results obtained for the Coma cluster, for which Zwicky concluded that additional mass was required to gravitationally bind the galaxies. We can make these results quantitative: from the virial theorem, for a gravitationally bound system, the time averaged kinetic energy $\langle K\rangle$ and potential energy $\langle V\rangle$ are related by

$$\langle K\rangle = -\frac{1}{2}\langle V\rangle. \tag{1.3}$$

Considering the one dimensional velocity dispersion of the galaxies, measured along the line of sight between the observer and the cluster, equal to $v_{\mathrm{los}} \sim 10^3$ km/s [14], and assuming an isotropic velocity distribution, we obtain the three dimensional dispersion

$$\langle v^2\rangle = 3\, v_{\mathrm{los}}^2. \tag{1.4}$$

Consequently, the time averaged kinetic energy can be expressed in terms of the total mass of the cluster M as

$$\langle K\rangle = \frac{1}{2} M\, \langle v^2\rangle. \tag{1.5}$$

Modeling the cluster as a sphere of total mass M, uniformly distributed within a radius R, the gravitational potential energy is given by

$$\langle V\rangle = -\frac{3\, G M^2}{5\, R}. \tag{1.6}$$

Substituting the expressions obtained for $\langle K\rangle$ and $\langle V\rangle$, respectively eq. (1.5) and eq. (1.6), into eq. (1.3) we can derive an expression for the mass of the cluster

$$\frac{1}{2}M\langle v^2\rangle = -\frac{1}{2}\left(-\frac{3}{5}\frac{GM^2}{R}\right) \qquad \Rightarrow \qquad M = \frac{5R\,\langle v^2\rangle}{3G} = \frac{5R\,v_{\rm los}^2}{G}. \tag{1.7}$$

To determine the value of M, we need to estimate the radius R, which can be obtained geometrically from the distance of the cluster from the Earth, $d \sim 100$ Mpc, and its angular radius $\theta \simeq 1°$ [15]. It is therefore possible to use the small-angle approximation

$$R \simeq d\,\theta \simeq 1.7 \text{ Mpc}. \tag{1.8}$$

Substituting $v_{\rm los} \sim 10^3$ km/s and $R \simeq 1.7$ Mpc into eq. (1.7), we obtain a total mass of the Coma cluster of the order of

$$M \simeq 2 \times 10^{15}\, M_\odot. \tag{1.9}$$

It is crucial to compare this value with the baryonic mass of the cluster, which is of the order of $10^{14}\, M_\odot$, obtained by summing the contribution from the visible mass of the $\sim 10^3$ galaxies and the hot gas measured through X-ray observations. It is thus observed that the mass responsible for the gravitational interaction is at least one order of magnitude larger than the estimated baryonic mass, implying the presence of additional, yet unknown, matter.

A further piece of evidence for the existence of DM comes from a system formed by two galaxy clusters in the process of colliding, known as the *Bullet cluster*, located 3.7 Gly away. As shown in fig. 1.3, X-ray emissions trace the regions where most of the baryonic matter is concentrated, which in this system is primarily in the form of hot gas. On the other hand, weak gravitational lensing allows the reconstruction of the total mass distribution of the system [16].

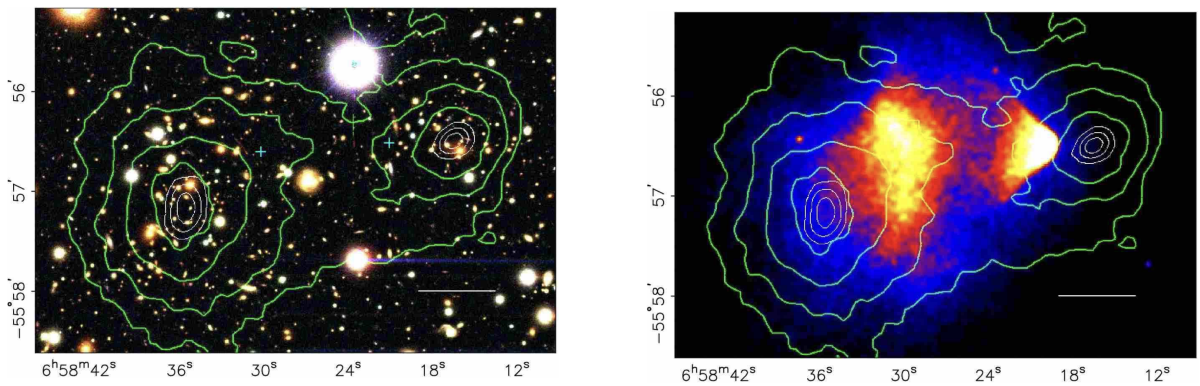

Figure 1.3: *Left panel: color image of the two merging clusters. Right panel: color map of the distribution of hot baryonic gas, reconstructed from X-ray emission. The green contours indicate the total mass distribution obtained through weak gravitational lensing. The white bar corresponds to a length of 200 kpc [16].*

The comparison between these observations reveals a clear separation between baryonic matter and the mass responsible for the gravitational interaction, once again suggesting the presence of additional matter. The special feature of the bullet cluster is that it shows the non-interacting nature of DM: it is supposed that in the past each of the two clusters had the visible matter and DM mixed together. The two objects collided 150 million years ago. Visible matter interacts significantly with itself, so that the hot gas from the two clusters experienced a collisional shock wave. DM, on the other hand, experienced negligible collisions with itself and with normal matter, such that it simply passed through.

These observations put a severe strain on alternative interpretations where DM is replaced by a modification of gravity, because such modifications cannot get spatially separated from normal matter. In the next section, these theories will nevertheless be briefly discussed.

Finally, moving to scales larger than galaxy clusters, it is important to mention the Cosmic Microwave Background (CMB) and the Large Scale Structures, which provide further evidence in support of DM on cosmological scales, where the most convincing and precise evidence is currently found. DM played a fundamental role as a catalyst in the formation of galaxies and galaxy clusters. Moreover, CMB temperature anisotropies would not look the way they do if it were not for DM. This was accurately studied by the Planck Collaboration, which measured the DM density from the analysis of the CMB power spectrum, obtaining $\Omega_c h^2 = 0.120 \pm 0.001$ [3].

1.2.3 Modified Newtonian Dynamics

In February 1982, Mordehai Milgrom submitted three papers [17, 18, 19] which provided the foundation for what would become the leading alternative to DM. Milgrom's proposal states that gravity, or inertia, does not follow the predictions of Newtonian dynamics for accelerations smaller than the characteristic acceleration $a_0 = 1.2 \times 10^{-8}$ cm/s^2, as derived from fits to galaxy rotation curves. The MOND gravitational acceleration a is related to the Newtonian acceleration a_N through an interpolation function $\mu(a/a_0)$, such that

$$a_N = a\,\mu\left(\frac{a}{a_0}\right), \tag{1.10}$$

where a_0 is meant to be a new constant of physics.

By construction, the interpolation function has the asymptotic behavior $\mu = 1$ for $a \gg a_0$, to recover the Newtonian expression in the strong field regime, and $\mu = a/a_0$ for $a \ll a_0$. In this limit, the gravitational acceleration becomes

$$a = \sqrt{a_N\, a_0} = \frac{\sqrt{GMa_0}}{r}, \tag{1.11}$$

with dependence $1/r$ instead of the Newtonian $1/r^2$ [20]. Within this framework, MOND successfully reproduces the flat rotation curves of galaxies. However, the value a_0 is introduced as an empirical parameter adjusted to match observational data. In fact, a large variation in a_0 is found studying different samples of galaxies. This shows that MOND works well as a fitting procedure but not as a universal description of gravity on the scale of galaxies [21].

Moreover, in its original formulation MOND suffered from several theoretical issues, such as the lack of energy conservation and the difficulty of a consistent relativistic extension. Subsequently, new theories were developed, such as the AQUAdratic Lagrangian (AQUAL) [22] and its relativistic extension RAQUAL, which are based on a Lagrangian formulation. Nevertheless, so far all these theories fail to provide a unified description capable of simultaneously explaining the full range of experimental observations.

1.3 Indirect detection

Indirect detection experiments aim to probe the nature of DM by searching for an excess (above the presumed astrophysical contribution) in the flux of SM particles produced through DM annihilation or decay. We show a schematic representation of the signal production mechanism in fig. 1.4. In this context, the most relevant messengers are photons (gamma rays and X-rays), neutrinos, and charged cosmic rays (such as positrons, antiprotons, antideuterons, and heavier antimatter nuclei). For charged cosmic rays, particular attention is given to antimatter particles since they are less likely to be produced in astrophysical processes than the corresponding matter particles, leading to a more favorable astrophysical background. However, their propagation through the Galaxy introduces additional systematic uncertainties, such as changes in their direction due to the galactic magnetic fields or energy losses while propagating.

First of all, we must assume that DM possesses at least one interaction channel producing SM particles. While there is no experimental confirmation of this, it is a natural expectation in well-motivated scenarios such as the "thermal relic" one, where the relic abundance is directly related to its annihilation cross section [23]. In alternative scenarios, in which DM annihilates or decays exclusively into itself, conventional indirect detection would not be effective.

The flux of cosmic rays produced by DM primarily depends on the annihilation cross section $\langle \sigma v \rangle$ or, in the case of decay, on the particle lifetime τ. Another crucial factor is the spatial distribution of DM, which enters through line of sight integrals called *J-factor*: the resulting flux is therefore expected to be enhanced in regions of higher DM density, such as the Galactic Center (GC) or dwarf spheroidal galaxies, although these environments might be challenging to study.

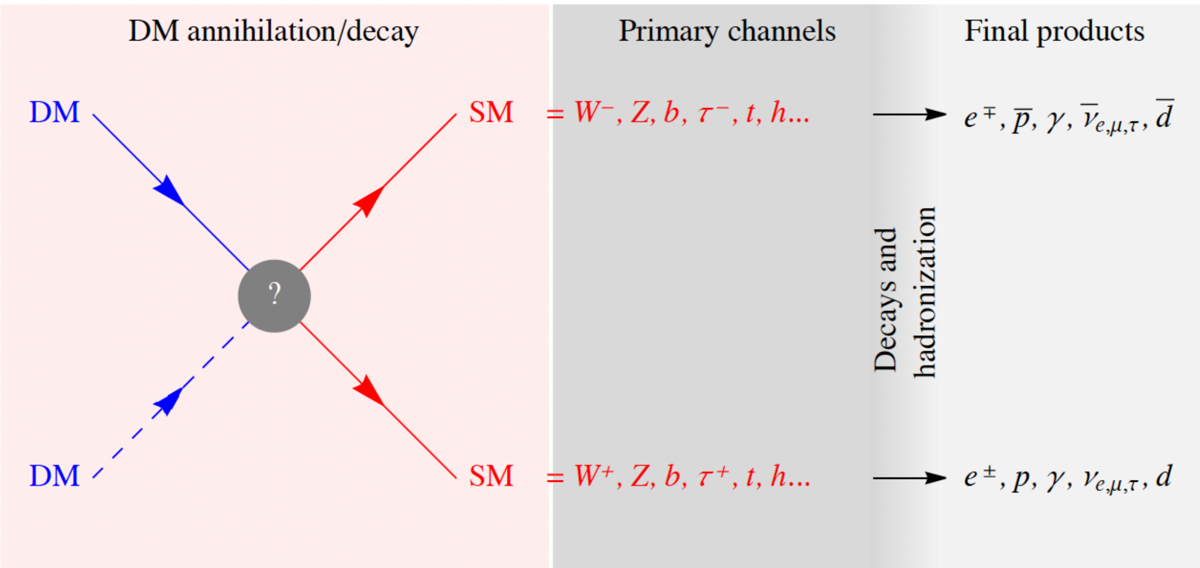

Figure 1.4: *Annihilation of DM into SM particles and generation of primary particle spectra [1].*

1.3.1 Gamma rays

The gamma-ray spectrum from DM annihilation can be classified according to its shape as follows

- γ-ray lines, from the direct annihilation of two DM particles into $\gamma\gamma$ or γX, e.g. with $X = Z$. In this case, the spectrum develops a prominent line centered at

$$E_\gamma = m_{\rm DM}\left(1 - \frac{m_X^2}{4\,m_{\rm DM}^2}\right), \tag{1.12}$$

which reduces to $E_\gamma = m_{\rm DM}$ in the $\gamma\gamma$ channel.

- γ-ray continuum, from prompt emission (hadronization and decay of annihilation products) and from secondary radiation processes.

Supposing a signal in gamma-ray lines is observed, then the size of the continuum with respect to the line and its spread in energy could allow one to distinguish between different models in explaining the origin of the line, if the relative background can be understood.

Through observations of γ-rays (high-energy photons), it is possible to derive some of the most stringent constraints on the DM annihilation cross section. The main advantage of gamma rays is the fact that photons are not deflected by magnetic fields and are negligibly attenuated over Galactic distance scales. This allows one to retain both spatial and spectral information, largely unaffected by astrophysical effects. Assuming self-conjugate DM, the differential γ-ray flux per unit solid angle and energy from DM annihilation, integrated over the line of sight s, can be written as

$$\frac{d\Phi_\gamma}{d\Omega\, dE} = \frac{1}{4\pi}\frac{1}{2m_{\rm DM}^2}\sum_f \langle\sigma v\rangle_f \frac{dN_{f\to\gamma}}{dE}\int_{\rm l.o.s.} ds\; \rho_{\rm DM}^2(\vec{r})\,. \tag{1.13}$$

This expression, derived in appendix A, connects the microphysical properties of DM to the astrophysical factors, which depend solely on the DM density profile along the line of sight. The quantity described by the integral in eq. (1.13) is often referred to as the J-factor, which encodes all of the relevant astrophysical information. In the particular case of the Milky Way (MW) we define a dimensionless J-factor, normalized over the distance from the Earth to the Galactic Center $r_\odot$ and the local DM density $\rho_\odot$

$$J_{\rm ann}(\theta) = \int_{\rm l.o.s.} \frac{ds}{r_\odot}\left(\frac{\rho_{\rm DM}(r(s,\theta))}{\rho_\odot}\right)^2. \tag{1.14}$$

The radial coordinate r is measured from the GC and is related to s through $r = \sqrt{r_\odot^2 + s^2 - 2\,r_\odot\, s\cos\theta}$. θ is the aperture angle between the direction of the line of sight and the axis linking the Earth to the GC.

Note that throughout this work we use both normalizations of the J-factor: the dimensionless definition of eq. (1.14), convenient to compare the angular shape of different profiles, and the dimensional definition, which is the line of sight integral in eq. (1.13), commonly adopted by experimental collaborations to quote limits. The two normalizations are simply related by

$$J^{\rm dim} = r_\odot\, \rho_\odot^2\, J_{\rm ann}. \tag{1.15}$$

The dimensionless J-factors for different DM profiles, most of which will be introduced and discussed later, are plotted in fig. 1.5 as a function of θ.

Equation (1.14) is useful if we need the flux of gamma rays from a given direction. Often we need instead the flux over solid angle regions, for example, an annulus centered around the GC with $\theta_{\min} < \theta < \theta_{\max}$

$$\Delta\Omega = 2\pi \int_{\theta_{\rm min}}^{\theta_{\rm max}} d\theta \, \sin\theta, \qquad \bar{J} = \frac{2\pi}{\Delta\Omega} \int_{\theta_{\rm min}}^{\theta_{\rm max}} d\theta \, \sin\theta \, J(\theta). \tag{1.16}$$

From the definition of the J-factor, one can infer the main features of ideal targets for DM detection: they should exhibit a high DM density, be located at relatively small distances, be spatially extended and feature a low or well-understood astrophysical background [24]. Dwarf spheroidal galaxies are particularly interesting because, although their J-factor is typically smaller than that of the inner volume of the Milky Way (the Galactic Center), they are characterized by a negligible astrophysical background. Nevertheless, they present some observational limitations: the so-called *ultra-faint dwarfs* allow spectroscopic analyses for only a limited number of stars and the low J-factor implies that years of studies are required to obtain sufficient data to draw meaningful conclusions. On the other hand, the Galactic Center is arguably the most promising source for DM annihilation in the Milky Way, unless the DM distribution exhibits a large core at its center. It presents, however, a large and not fully understood astrophysical background.

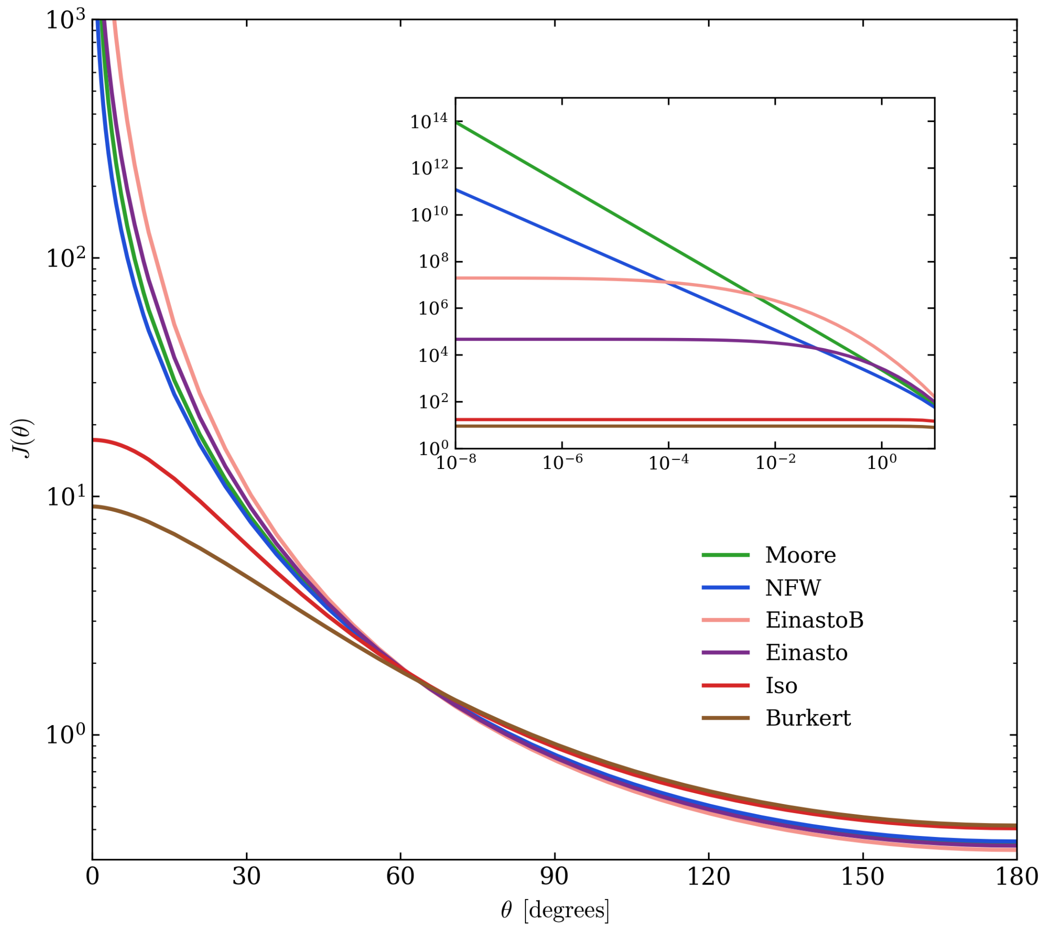

Figure 1.5: *Dimensionless J-factors for different DM profiles. From top to bottom, the color identifies the profiles: Moore [25], NFW [9, 10], EinastoB (α = 0.11), Einasto (α = 0.17) [26], Iso [27], Burkert [28]. Functional forms from [29]. The J-factors are computed with the profiles normalized to $\rho_\odot = 0.4$ GeV/cm^3 at $r_\odot = 8.33$ kpc and $M(< 60\ \text{kpc}) = 4.7 \times 10^{11}\, M_\odot$, as in the rest of this work. See section 2.1 for more details on the calculation.*

In the next chapter we compute the J-factors for different DM density profiles and derive quantitative constraints on the annihilation cross section in the region of the Galactic Center.

Chapter 2

Dark matter constraints from the Galactic Center

The Galactic Center is expected to be the single brightest source of DM annihilation products on the sky. In particular, using a standard NFW profile, shown in eq. (1.2), with $r_s = 20$ kpc and a local density of 0.4 GeV/cm^3, from eq. (1.13) we obtain a flux of gamma rays that is more than three orders of magnitude larger than that predicted from the brightest dwarf galaxies [24]. However, the mass within the innermost kpc of the Milky Way is dominated by baryons, this leads to a higher astrophysical background and, most importantly, numerical simulations need to include hydrodynamics and feedback physics in addition to the gravitational effects, resulting in uncertainties in the obtained DM profiles towards the GC. These simulations agree that the DM profile of MW-like galaxies develops a peak towards the Galactic Center but their resolution prevents them from determining a well-defined DM distribution.

Therefore, in this chapter we define a set of representative DM density profiles, determine their parameters from observational constraints and compute their J-factors. Then, we introduce a simple model of thermal relic DM and confront it with the upper limits on the annihilation cross section obtained by the H.E.S.S. Inner Galaxy Survey [2], showing how different profiles lead to different constraints.

2.1 Dark matter density profiles and J-factors

As long as a clearer determination of the DM profile in the inner Milky Way regions is not achieved, it is worth considering a range of possible choices and comparing them. In particular, the two limiting cases are: a peaked profile, in which the density keeps rising steeply towards the GC, and a cored one, in which the density flattens to a finite central value. Therefore, in what follows we consider the Einasto (peaked) [26], Burkert (cored) [28] and NFW [9, 10] with a variable core radius r_c as representative DM density profiles $\rho_{\rm DM}(r)$.

For the Einasto profile the functional form reads

$$\rho_{\rm Ein}(r) = \rho_s \exp\left[-\frac{2}{\alpha}\left(\left(\frac{r}{r_s}\right)^{\alpha} - 1\right)\right], \tag{2.1}$$

where $\alpha = 0.17$ is a shape parameter that controls how the logarithmic slope of the density varies with the radius. Note that the Einasto profile does not diverge for small radii, nevertheless, in the region of our analysis it behaves as a peaked profile.

The Burkert profile is

$$\rho_{\rm Bur}(r) = \frac{\rho_s}{\left(1+\dfrac{r}{r_s}\right)\left(1+\left(\dfrac{r}{r_s}\right)^2\right)}, \tag{2.2}$$

which flattens to ρ_s at small radii, defining a core of size $\sim r_s$.

The functional form of the cored NFW is

$$\rho_{\rm NFW}(r, r_c) = \begin{cases} \rho_s \dfrac{r_s}{r_c} \dfrac{1}{\left(1+\dfrac{r_c}{r_s}\right)^2} & \text{for } r \leq r_c \\ \rho_s \dfrac{r_s}{r} \dfrac{1}{\left(1+\dfrac{r}{r_s}\right)^2} & \text{for } r > r_c \end{cases} \tag{2.3}$$

Once r_c is fixed, all three profiles depend on two free parameters, ρ_s and r_s. We determine them by fitting the DM density at the Sun's position: $\rho(r_\odot = 8.33 \text{ kpc}) = 0.4 \text{ GeV/cm}^3$ [30], and the total DM mass within 60 kpc: $M(< 60 \text{ kpc}) = 4.7 \times 10^{11}\, M_\odot$ [31]. For the NFW profile these conditions yield $r_s \simeq 14.0$ kpc and $\rho_s \simeq 0.60 \text{ GeV/cm}^3$, these values will be adopted throughout this work.

In order to make a more quantitative description, we compute the corresponding J-factors, as done in [31]. From now on, we adopt the dimensional definition of the J-factor in order to properly compare our results with the experimental values. The main difference with [31] is the DM density at the Sun's position: they adopt $\rho(r_\odot) = 0.3 \text{ GeV/cm}^3$, while here we use $\rho(r_\odot) = 0.4 \text{ GeV/cm}^3$, since recent studies consider this value more accurate. Improved determinations of the local DM density are being carried out, see [30] for instance. As a check, we verified that setting $\rho(r_\odot) = 0.3 \text{ GeV/cm}^3$ reproduces the values reported in [31]. We integrate the J-factors over an angular region, centered on the GC, defined as

$$\Omega_{\rm obs} = \Omega(\theta < 1^\circ,\ |b| > 0.3^\circ), \tag{2.4}$$

where $\theta > 0^\circ$ is the polar angle with respect to the GC direction and b is the galactic latitude with respect to the disk plane. At the Sun's distance $r_\odot = 8.33$ kpc, the angles 1° and 0.3° correspond to projected distances of approximately 145 pc and 44 pc from the GC, respectively. The $|b| > 0.3^\circ$ cut is motivated by the choice of [2] to mask the large photon backgrounds from the galactic ridge. The results are reported in table 2.1, where we use three illustrative values of r_c for the cored NFW.

	Einasto	Burkert	$\text{NFW}_{30\,\text{pc}}$	$\text{NFW}_{300\,\text{pc}}$	$\text{NFW}_{3\,\text{kpc}}$
ρ_s [GeV/cm^3]	0.171	1.283	0.604	0.604	0.586
r_s [kpc]	12.9	9.7	14.0	14.0	14.3
$\log_{10}\left(J_{\Omega_{\rm obs}}\left[\dfrac{\text{GeV}^2}{\text{cm}^5}\right]\right)$	21.96	19.35	21.57	21.16	19.77

Table 2.1: *Values of the parameters ρ_s and r_s obtained from the fitting conditions, and J-factors for DM annihilation integrated over the region $\Omega_{\rm obs}$ of eq. (2.4), centered on the Galactic Center, for the Einasto, Burkert and cored NFW density profiles, with the NFW core radii r_c reported as subscripts.*

The values in table 2.1 span more than two orders of magnitude between the Einasto profile, the most peaked one, and Burkert, the most cored one. This has a direct consequence for the upper bounds on the DM annihilation cross section: since the predicted flux scales linearly with the J-factor, the upper bound on $\langle \sigma v \rangle$ is inversely proportional to it. Consequently, a more peaked profile yields a stronger constraint, namely a lower upper limit on the cross section, than a cored one. In particular, the upper bound on $\langle \sigma v \rangle$ derived under the Burkert assumption is roughly a factor $\sim 4 \times 10^2$ weaker than the one obtained under Einasto.

This shows that, when the analysis is restricted to regions very close to the Galactic Center, the uncertainty on the DM density profile has a very large impact on the constraints on the annihilation cross section. Instead, if a larger region of observation is considered, the impact of this uncertainty is reduced, since the different profiles show a similar behavior in outer regions. On the other hand, restricting the region of observation can reduce the astrophysical backgrounds. This is the reason why small regions close to the GC are particularly interesting for indirect searches, in particular for the study of DM spikes.

2.2 Thermal relic cross section and indirect detection constraints

We now consider the model where two DM particles χ annihilate into two BSM mediators ϕ, i.e. particles that are not SM,

$$\chi\chi \to \phi\phi. \tag{2.5}$$

The mediators are then assumed to later decay into SM particles.

In the following calculation we use natural units, where $\hbar = c = 1$, masses and energies are expressed in GeV and cross sections in GeV^{-2}.

The annihilation cross section for the process $\chi\chi \to \phi\phi$ is [1]

$$\langle \sigma v \rangle_{\chi\chi\to\phi\phi} = \frac{\pi \alpha_D^2}{m_{\mathrm{DM}}^2}, \tag{2.6}$$

where m_{DM} is the DM mass and α_D is the coupling constant of the dark sector, defined as

$$\alpha_D = \frac{g_D^2}{4\pi}, \tag{2.7}$$

with g_D the coupling between the BSM mediators and DM.

Assuming the thermal relic scenario, the observed DM abundance is obtained for an annihilation cross section of order $10^{-26}\,\mathrm{cm}^3/\mathrm{s}$. For a quantitative analysis, we use the value for self-conjugate DM with mass greater than 10 GeV [32]

$$\langle \sigma v \rangle = 2.2 \times 10^{-26}\ \mathrm{cm}^3/\mathrm{s} \simeq 1.89 \times 10^{-9}\ \mathrm{GeV}^{-2}. \tag{2.8}$$

From eq. (2.6) we can easily compute the value of $\alpha_D(m_{\mathrm{DM}})$ that gives the correct relic abundance

$$\alpha_D(m_{\mathrm{DM}}) \simeq 2.45 \times 10^{-5} \left(\frac{m_{\mathrm{DM}}}{\mathrm{GeV}}\right) \simeq 0.0245 \left(\frac{m_{\mathrm{DM}}}{1\ \mathrm{TeV}}\right). \tag{2.9}$$

Once α_D is chosen, the annihilation cross section of our model is fixed.

We now assume that the mediators decay into W bosons, therefore the complete process is

$$\chi\chi \to \phi\phi \to W^+W^- \, W^+W^- . \tag{2.10}$$

For simplicity, we use the limit for DM annihilating directly into the W^+W^- channel.

This is a good approximation because, as discussed in section 1.3.1, the γ-ray spectrum from W hadronization is a broad continuum: the extra step through the mediators halves the average energy of each W and doubles their multiplicity, but this mildly affects the spectrum.

To constrain our model, in what follows we employ the experimental upper limits on the DM annihilation cross section obtained by the H.E.S.S. experiment. The High Energy Stereoscopic System (H.E.S.S.) is an array of Imaging Atmospheric Cherenkov Telescopes located in the Khomas Highland of Namibia, sensitive to very-high-energy γ-rays from a few tens of GeV to several tens of TeV [33]. It does not detect the γ-rays directly: when a very-high-energy photon enters the atmosphere it initiates an electromagnetic cascade of secondary particles that travel faster than the speed of light in air and therefore emit a faint, nanosecond-long flash of Cherenkov light. Each telescope records an image of this flash, and the combination of the images taken simultaneously, a technique known as stereoscopy, allows the arrival direction and the energy of the primary photon to be reconstructed with high accuracy. In this way the instrument effectively measures the γ-ray flux and energy spectrum coming from a given region of the sky, which is precisely the observable that can be compared with the signal predicted from DM annihilation. The performance of the array, in terms of angular and energy resolution and sensitivity, was established through the observation of the Crab Nebula, the standard candle of very-high-energy γ-ray astronomy [34]. Owing to its location in the southern hemisphere, H.E.S.S. observes the Galactic Center at small zenith angles, close to the optimal observing conditions, which makes it one of the leading instruments for indirect DM searches at the TeV scale.

In particular, Ref. [2] provides 95% confidence level (C.L.) upper limits on the annihilation cross section $\langle \sigma v \rangle_{\rm lim}(m_{\rm DM})$ as a function of the DM mass. H.E.S.S. adopts an NFW profile with $\rho_\odot = 0.39$ GeV/cm^3 at $r_\odot = 8.5$ kpc and $r_s = 21$ kpc, while we adopt the parameters determined in section 2.1: $\rho_\odot = 0.4$ GeV/cm^3 at $r_\odot = 8.33$ kpc and $r_s \simeq 14.0$ kpc. We can adjust these limits using our parameters by rescaling them with the ratio of the J-factors for the two sets of parameters, both computed over the region of observation of the Inner Galaxy Survey, $0.5° < \theta < 3°$ with $|b| > 0.3°$, which in this case gives $J^{\rm H.E.S.S.}/J^{\rm our} \simeq 0.60$.

Since the expected gamma-ray flux is proportional to $\langle \sigma v \rangle J$, a cored NFW profile, having a smaller central DM density and hence a smaller J-factor, leads to a weaker limit. Rescaling the NFW limit by the ratio of the J-factors, we obtain

$$\langle \sigma v \rangle^{\rm cored}_{\rm lim} \simeq \langle \sigma v \rangle^{\rm NFW}_{\rm lim} \frac{J_{\rm NFW}}{J_{\rm cored}}, \tag{2.11}$$

where $J_{\rm NFW}/J_{\rm cored} \simeq 4.0$ for a flat core of radius $r_c = 1$ kpc. Therefore, the limit obtained under the cored assumption is weaker than the one obtained under NFW,

$$\langle \sigma v \rangle^{\rm cored}_{\rm lim} > \langle \sigma v \rangle^{\rm NFW}_{\rm lim}. \tag{2.12}$$

The resulting limits are shown in fig. 2.1 for the NFW and the cored NFW profiles, together with the thermal relic cross section of our model. We focus on the NFW and cored NFW profiles since the H.E.S.S. experimental limits we employ are provided for the NFW profile.

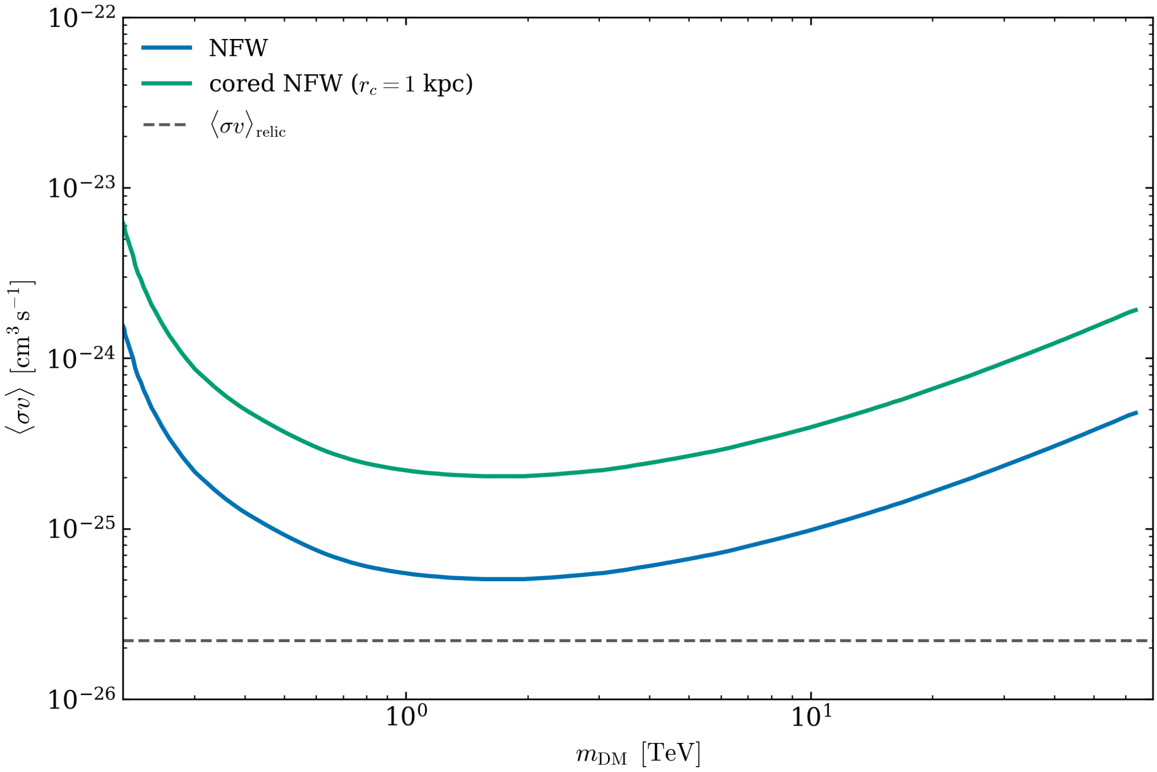

Figure 2.1: *95% C.L. upper limits on the annihilation cross section in the W^+W^- channel from the H.E.S.S. Inner Galaxy Survey [2], rescaled to our halo parameters. We adopt the NFW and the cored NFW profiles. The dashed line is the cross section that reproduces the observed relic abundance in our model.*

It is useful to discuss the relation between the number of photons detected and the DM mass in order to understand the shape of the limit curves. Recalling eq. (1.13), we notice that the γ-ray flux scales as

$$\Phi \propto \frac{\langle\sigma v\rangle}{m_{\rm DM}^2}\, J \int_{E_{\rm thr}}^{m_{\rm DM}} \frac{dN_{f\to\gamma}}{dE}\, dE, \tag{2.13}$$

where $E_{\rm thr}$ is the energy threshold of the telescope and the spectrum extends up to $E \simeq m_{\rm DM}$. The upper limit $\langle\sigma v\rangle_{\rm lim}$ is inversely proportional to the number of detectable photons per annihilation, hence we can distinguish three different regimes.

At low masses, most of the photons produced fall below $E_{\rm thr}$ and are lost, therefore the limit is weak and the curve rises for small $m_{\rm DM}$.

At intermediate masses, of the order of a TeV, the photon spectrum falls in the energy range where H.E.S.S. is most sensitive, and the limit reaches its strongest value, which corresponds to the minimum of the curve.

At high masses, the telescopes are still able to detect most of the photons, but the annihilation rate is suppressed by the factor $1/m_{\rm DM}^2$ of eq. (2.13): at fixed mass density, the number density of DM particles decreases as ρ/m_{DM}, and two particles are needed for each annihilation, therefore the upper limit curve rises.

We can compare the cross section predicted by our model with the experimental upper limit and exclude the DM mass values that give a cross section larger than the upper limit. Since our model predicts a constant cross section after imposing the relic abundance, the condition of exclusion becomes

$$2.2 \times 10^{-26}\ \mathrm{cm}^3/\mathrm{s} > \langle \sigma v \rangle_{\mathrm{lim}}(m_{\mathrm{DM}}). \tag{2.14}$$

From fig. 2.1 we can evaluate this condition: if the upper limit lies below the thermal relic value, the corresponding DM mass is excluded. If it lies above the thermal relic value, the model is still allowed.

Figure 2.1 also shows how the upper limit changes when different DM density profiles are assumed.

For the NFW profile, the thermal relic cross section lies below the upper limit at all masses, so no value of m_{DM} is excluded within this approximation. Since the cored NFW yields an even weaker limit, as shown in eq. (2.11), the same conclusion holds for the cored profile: the thermal relic model is not excluded in either case.

It is important to notice that in this case we are assuming that our relic model is correct and then excluding the different DM masses and density profiles. Strictly speaking, the rigorous interpretation is that a point $(m_{\mathrm{DM}}, \langle \sigma v \rangle)$ above the limit curve is excluded in the sense that the three hypotheses, which are the DM profile, mass and cross section, are simultaneously incompatible. In our work we fix the cross section since it is a robust theoretical prediction, while the DM density profile is affected by numerous uncertainties, which will be discussed in detail in the next chapter.

Chapter 3

Spikes in dark matter density profiles

There is strong evidence for the presence of a supermassive black hole (SMBH or simply BH), called Sgr A*, at the center of our Galaxy.

The first dynamical calculation of its mass came from Eckart and Genzel [35] and Ghez et al. [36], who studied the stellar velocity dispersion in the inner 0.1 pc and estimated the mass of Sgr A* to be $M_{\mathrm{BH}} = (2.6 \pm 0.2) \times 10^6\, M_\odot$. New measurements have been done by tracking the complete orbits of individual stars around Sgr A*, for instance see [37, 38]. The most precise determination to date, obtained by the GRAVITY interferometer from the orbit of the star S2, is $M_{\mathrm{BH}} = (4.15 \pm 0.01) \times 10^6\, M_\odot$ [39].

If cold DM is present at the Galactic Center, as in current models of the dark halo, the adiabatic growth of the black hole redistributes it into a cusp, called a *spike*. From eq. (1.13) we have seen that the annihilation rate depends on the square of the DM density, so it is strongly increased in the spike. The absence of a detected signal then allows one to place interesting upper limits on the density slope of the inner halo, under the assumption of DM being a thermal relic. However, the determination of the DM density profile in the spike is affected by severe uncertainties.

Therefore, in this chapter we study the formation of DM spikes around black holes, derive the relation between the slope of the spike and that of the DM halo, examining its physical origin and its regime of validity, and discuss the main astrophysical uncertainties affecting the spike profile. Finally, we compute the J-factors for DM annihilation around the Galactic Center for two benchmark spike profiles, on both a peaked NFW and a cored halo.

3.1 Adiabatic spike around the central black hole

We want to find the DM density profile in the region where the black hole dominates the gravitational potential. From the data in [35, 36], Gondolo and Silk [40] estimated this region to be of the order of a parsec.

We work under the assumption that the growth of the black hole is adiabatic: this means that the black hole grows on a time scale much longer than the typical orbital time of the DM particles in the central region. This assumption is supported by the collisionless behavior of particle DM, discussed in section 1.1.

In order to determine the DM density profile after the formation of the black hole, it is useful to describe the system in terms of the phase-space distribution $f(\mathbf{x}, \mathbf{v})$, defined as the DM mass per unit phase-space volume, recalling the relation

$$\rho(\mathbf{x}) = \int f(\mathbf{x}, \mathbf{v}) \, d^3v, \tag{3.1}$$

which means that the density at a point is obtained by integrating the DM mass per unit phase-space volume over all velocities. With this convention ρ is the mass density, in GeV/cm^3, and the corresponding number density is ρ/m_{DM}.

For a spherically symmetric system we can express the phase-space distribution as a function of the energy E and the angular momentum L of the particles. While the density profile gives information about the amount of DM at a given position, $f(E, L)$ contains additional information on the orbital structure of the system.

Therefore, the final DM density profile can be calculated by integrating the final phase-space distribution $f'(E', L')$ over all the bound orbits that pass through a radius r

$$\rho'(r) = \int_{E'_m}^{0} dE' \int_{L'_c}^{L'_m} dL' \, \frac{4\pi L'}{r^2 v_r} \, f'(E', L'), \tag{3.2}$$

where E' and L' are respectively the final energy and angular momentum per unit mass, and

$$v_r = \left[2\left(E' + \frac{GM_{\mathrm{BH}}}{r} - \frac{L'^2}{2r^2}\right)\right]^{1/2} \tag{3.3}$$

is the radial velocity. The derivation of this expression is reported in appendix B.1.

The integration limits are

$$E'_m = -\frac{GM_{\mathrm{BH}}}{r}\left(1 - \frac{4R_{\mathrm{S}}}{r}\right), \qquad L'_c = 2cR_{\mathrm{S}}, \qquad L'_m = \left[2r^2\left(E' + \frac{GM_{\mathrm{BH}}}{r}\right)\right]^{1/2}. \tag{3.4}$$

The upper bound for the energy is $E' = 0$, which means we are neglecting the contribution from unbound orbits. The lower limit in angular momentum L'_c and the second factor in E'_m eliminate the particles with $L < 2cR_S$, where $R_S = \frac{2GM_{\mathrm{BH}}}{c^2}$ is the Schwarzschild radius. These particles have angular momentum small enough to be captured by the black hole, so they have to be excluded. The angular momentum upper bound is obtained from the condition that the radial velocity must be real.

The key point is that, in the adiabatic approximation, we relate the final phase-space distribution $f'(E', L')$ to the initial one $f(E, L)$ through the conservation of the angular momentum and of the radial action. The angular momentum is conserved because the potential remains spherically symmetric during the growth of the black hole. Moreover, since the potential varies on a time scale much longer than the orbital periods, the radial action

$$I(E, L) = \oint v_r \, dr = 2\int_{r_-}^{r_+} v_r \, dr, \tag{3.5}$$

where $r_\pm$ are the turning points of the orbit, is also conserved. This is a classical result on adiabatic invariants, see e.g. [41]. The conservation of the phase-space density along the orbits follows from Liouville's theorem. Finally, we have

$$f'(E', L') = f(E, L), \qquad L' = L, \qquad I'(E', L') = I(E, L). \tag{3.6}$$

This means that the growth of the black hole does not create DM particles, it only modifies their orbits, increasing their density in the central region and forming a spike.

3.2 Relation between the slope of the spike and that of the DM halo

We now want to derive the relation between the slope of the spike and that of the DM halo. For this purpose, we follow the procedure of Ullio, Zhao and Kamionkowski [42], which reproduces the original result of Gondolo and Silk [40].

3.2.1 Halo distribution with only circular orbits

Before the general treatment, it is instructive to consider a simple toy model that illustrates the origin of the Gondolo–Silk spike.

We assume an initial self-gravitating DM distribution

$$\rho(r) = \rho_s \left(\frac{r}{r_s}\right)^{-\gamma}, \qquad 0 < \gamma < 2, \tag{3.7}$$

made of particles that are all on circular orbits, at the center of which a black hole grows adiabatically. Note that here, and throughout this section, we neglect the gravitational effect of the baryonic components and consider only that of DM and black hole. We consider the more realistic scenario in which baryonic components are included in section 3.3.2.

The enclosed mass and the angular momentum of a circular orbit of radius r_i are

$$M(r_i) \propto r_i^{3-\gamma}, \qquad L_i^2 = G\, M(r_i)\, r_i \propto r_i^{4-\gamma}. \tag{3.8}$$

After the growth of the black hole, the mass enclosed within the final radius r_f is dominated by the BH at small radii: $M_f(r_f) \simeq M_{\rm BH}$ as $r_f \to 0$, so $L_f^2 = GM_{\rm BH}\, r_f$. Since the black hole exerts no torque on any DM particle, the angular momentum is conserved ($L_i = L_f$) and we obtain the relation

$$r_f \propto r_i^{4-\gamma}. \tag{3.9}$$

Each orbit shrinks by a factor $r_f/r_i \sim M(r_i)/M_{\rm BH}$: for the innermost orbits the contraction is huge, since $M(r_i) \ll M_{\rm BH}$, while orbits that enclose a mass larger than $M_{\rm BH}$ are practically unaffected. Therefore, we conclude that the spike is made up of particles from the region of the halo that initially enclosed a mass roughly equal to $M_{\rm BH}$, for an NFW halo this is the inner ~ 50 pc [42]. It is important to note that these particles are initially very cold, since $v_c \to 0$ as $r \to 0$.

We can obtain the final density profile from the conservation of mass shell by shell

$$\rho_f(r_f)\, r_f^2\, dr_f = \rho_i(r_i)\, r_i^2\, dr_i \tag{3.10}$$

and writing $\rho_f \propto r_f^{-\gamma_{\rm sp}}$ we get

$$r_f^{3-\gamma_{\rm sp}} \propto r_i^{3-\gamma}. \tag{3.11}$$

Now, using eq. (3.9), we obtain the final slope of the spike for our toy model

$$3-\gamma = (4-\gamma)\,(3-\gamma_{\rm sp}) \qquad \Longrightarrow \qquad \gamma_{\rm sp} = \frac{9-2\gamma}{4-\gamma}. \tag{3.12}$$

In the following, we will obtain the same result in a more rigorous and complete way.

3.2.2 General scaling relation

We now consider again the adiabatic growth of the black hole and the phase-space treatment introduced previously.

We adopt the general family of spherical double-power-law DM density profiles, introduced by Zhao [43],

$$\rho(r) = \rho_s \left(\frac{r}{r_s}\right)^{-\gamma} \left[1 + \left(\frac{r}{r_s}\right)^{\alpha}\right]^{-(\beta-\gamma)/\alpha}, \tag{3.13}$$

where γ is the inner slope, for $r \ll r_s$, β the outer slope, for $r \gg r_s$, r_s is the scale radius of the halo and α controls the sharpness of the transition between the two regimes.

Note how this family contains all the cases of interest: for $(\alpha, \beta, \gamma) = (1, 3, 1)$ we recover the NFW profile, $\gamma = 0$ corresponds to cored halos and for $\beta = \gamma$ we have the toy model profile of eq. (3.7).

For $r \ll r_s$ the density approaches $\rho_s(r/r_s)^{-\gamma}$ and we can obtain the functional form of the initial potential near the center from Poisson's equation (see appendix B.2 for the full derivation)

$$\phi(r) \simeq \phi_0 \left(\frac{r}{r_s}\right)^{2-\gamma}, \tag{3.14}$$

where, without loss of generality, we have fixed the value of the initial gravitational potential at the center to zero: $\phi(0) = 0$, possible since the potential is finite at the center for $\gamma < 2$. Note that with $\phi(0) = 0$ the potential increases outward and every orbit of the initial halo is bound, with $E > 0$. The most bound particles are those closest to the center and with $E \to 0^+$.

Equation (3.14) is the leading behavior of the potential for any density profile with inner slope γ, with $0 \leq \gamma < 2$. Note that the case $\gamma = 0$ is allowed and leads to a harmonic potential ($\phi \propto r^2$).

We also assume, following [42], that the final potential is dominated by the black hole in its vicinity, while it is roughly unchanged at large galactocentric distances, fixing

$$\phi'(r) \simeq \phi(r) - \frac{GM_{\rm BH}}{r}. \tag{3.15}$$

We postulate that the initial halo has an isotropic velocity distribution, this means that the phase-space distribution depends only on the energy ($f = f(E)$) and there is a one-to-one correspondence between the density profile and the distribution function given by Eddington's formula [41, 42]

$$f(E) = \frac{1}{\sqrt{8}\,\pi^2} \frac{d}{dE} \int_E^{\infty} \frac{d\rho}{d\phi} \frac{d\phi}{\sqrt{\phi - E}}. \tag{3.16}$$

Eddington's formula is derived in appendix B.3 following section 4.3 of [41].

To proceed we need a relation between initial and final energies, which can be obtained from the conservation of the radial action. For the initial potential we need to make some dimensional considerations, sufficient to determine the scaling. A particle with energy E can have an orbit with maximum radius r_E defined by

$$\phi(r_E) \sim E \tag{3.17}$$

and from the functional form of the potential it follows that $r_E \propto E^{1/(2-\gamma)}$, with a typical velocity $v \sim \sqrt{E}$, so that

$$I(E,L) = \oint v_r \, dr \sim r_E \sqrt{E} \propto E^{\frac{1}{2-\gamma}} \cdot E^{\frac{1}{2}} = E^{\frac{4-\gamma}{2(2-\gamma)}}. \tag{3.18}$$

In the final potential the radial action is known exactly

$$I'(E',L') = 2\pi \left(-L' + \frac{GM_{\rm BH}}{\sqrt{-2E'}} \right), \tag{3.19}$$

and for small radii the second term dominates so $I' \propto (-E')^{-1/2}$.

Both results for the initial and final potential are derived in detail in appendix B.4.

Now applying the conservation of the radial action we obtain

$$E \propto (-E')^{-\frac{2-\gamma}{4-\gamma}}, \tag{3.20}$$

which is the scaling relation between initial and final energies, first obtained in [44].

Note that, due to the definition of the initial and final potential, the most bound final orbits are the ones with $E' \to -\infty$, which populate the innermost region of the spike, and correspond to the initially most bound orbits with $E \to 0^+$.

Now supposing that the distribution function in the initial state diverges near the center as

$$f(E) \sim E^{-n}, \qquad E \to 0^+, \tag{3.21}$$

we can derive the final density profile at small radii, in the region where the potential is dominated by the black hole. There $\phi'(r) \simeq -GM_{\rm BH}/r$, and bound particles have $E' = -GM_{\rm BH}/r + v^2/2$ with $0 \leq v \leq v_{\rm esc} = \sqrt{2GM_{\rm BH}/r}$.

Note that here we introduce n only as an assumption on the behaviour of f, it is not a free parameter: in section 3.2.3 we derive it as a function of the problem data for a specific power-law ρ, and in section 3.2.4 for the general profile of eq. (3.13) introduced above.

The final distribution function is obtained recalling the consideration made in section 3.1, in particular from Liouville's theorem

$$f'(E') = f(E(E')) \propto (-E')^{n\frac{2-\gamma}{4-\gamma}}, \tag{3.22}$$

and integrating over the velocity space (see appendix B.5 for the explicit integral)

$$\rho'(r) = 4\pi \int_0^{v_{\rm esc}} f'\left(-\frac{GM_{\rm BH}}{r} + \frac{v^2}{2} \right) v^2 \, dv \;\propto\; \left(\frac{GM_{\rm BH}}{r} \right)^{n\frac{2-\gamma}{4-\gamma}} \left(\frac{GM_{\rm BH}}{r} \right)^{3/2}, \tag{3.23}$$

where the first factor comes from the scaling of f' and the second from the phase-space volume $\sim v_{\rm esc}^3$. We therefore obtain the general scaling relation

$$\rho'(r) \propto r^{-\gamma_{\rm sp}}, \qquad \gamma_{\rm sp} = \frac{3}{2} + n\,\frac{2-\gamma}{4-\gamma}. \tag{3.24}$$

This result shows that the slope of the spike is not only determined by the halo slope γ, but by the pair (γ, n), where n determines the strength of the divergence of the phase-space distribution on the most bound orbits. Particularly important is the case of $n = 0$, which means that $f(E)$ approaches a finite constant, as in models with a core: the spike slope is $\gamma_{\rm sp} = 3/2$ for any γ.

3.2.3 The Gondolo–Silk spike

Gondolo and Silk [40] studied in particular a single power law density profile (the same we examined in section 3.2.1)

$$\rho(r) = \rho_s \left(\frac{r}{r_s}\right)^{-\gamma}, \tag{3.25}$$

which is the general family of eq. (3.13) with $\beta = \gamma$ and $0 < \gamma < 2$.

For this profile the initial potential of eq. (3.14) is exact at all radii, so we can recover all the scaling results obtained previously and complete them deriving the normalization of the profile and the shape near the boundaries.

We do that integrating Poisson's equation and, recovering the results obtained in appendix B.2, we have

$$\phi(r) = \frac{4\pi G\rho_s r_s^\gamma}{3-\gamma}\int_0^r r'^{1-\gamma}\,dr' = \phi_0\left(\frac{r}{r_s}\right)^{2-\gamma}, \qquad \phi_0 = \frac{4\pi G\rho_s r_s^2}{(3-\gamma)(2-\gamma)}. \tag{3.26}$$

so that

$$\rho \propto \phi^{-\frac{\gamma}{2-\gamma}} \tag{3.27}$$

and Eddington's formula of eq. (3.16) can be evaluated exactly, the computation is reported in appendix B.6, giving a pure power law

$$f(E) = \frac{\rho_s}{(2\pi\phi_0)^{3/2}}\frac{\Gamma(n)}{\Gamma\left(n-\frac{3}{2}\right)}\left(\frac{\phi_0}{E}\right)^n, \qquad n = \frac{6-\gamma}{2(2-\gamma)}. \tag{3.28}$$

Inserting this value of n into eq. (3.24),

$$\gamma_{\text{sp}} = \frac{3}{2} + \frac{6-\gamma}{2(2-\gamma)}\cdot\frac{2-\gamma}{4-\gamma} = \frac{9-2\gamma}{4-\gamma}, \tag{3.29}$$

which is the famous result of Gondolo and Silk.

To find the final phase-space distribution $f'(E', L')$ we need to solve the equation of conservation of the radial action $I(E, L) = I'(E', L')$ for E as a function of E'. We already derived the final radial action, after the formation of the black hole, which is

$$I'(E', L') = 2\pi\left(-L' + \frac{GM_{\text{BH}}}{\sqrt{-2E'}}\right). \tag{3.30}$$

But in the initial power law potential the action integral cannot be performed exactly. Gondolo and Silk therefore performed this inversion numerically, finding an approximation accurate to better than 8% for $0 < \gamma < 2$.

So, once the relation between the initial and final energy is known, it is possible to integrate eq. (3.2) with the final distribution $f'(E', L') = f(E(E', L'))$, obtaining the complete density profile of the spike

$$\rho'(r) = \rho_R\, g_\gamma(r)\left(\frac{R_{\text{sp}}}{r}\right)^{\gamma_{\text{sp}}}, \qquad \gamma_{\text{sp}} = \frac{9-2\gamma}{4-\gamma}, \tag{3.31}$$

where

$$\rho_R = \rho_s \left(\frac{R_{\rm sp}}{r_s}\right)^{-\gamma}, \qquad R_{\rm sp} = A_\gamma\, r_s \left(\frac{M_{\rm BH}}{\rho_s r_s^3}\right)^{1/(3-\gamma)}. \tag{3.32}$$

Here ρ_R is the density normalization, $R_{\rm sp}$ is the radius of the spike, A_γ is a normalization factor and $g_\gamma(r) \simeq (1-4R_S/r)^3$ accounts for the capture of particles by the black hole. Therefore, the density vanishes for $r < 4R_S$. It is important to note that the factor $g_\gamma(r)$ follows from the Newtonian treatment of capture adopted in [40]. Adopting a relativistic description of the adiabatic growth of the spike [45] shows that the spike actually extends down to $2R_{\rm S}$. Throughout this work we will adopt the conservative cutoff at $4R_{\rm S}$.

For $0 < \gamma < 2$, the density slope in the spike varies only between 2.25 and 2.5: we note that the spike is always much steeper than the initial cusp.

Note that, for $\gamma \to 0$ we have $n \to 3/2$ from eq. (3.28), and studying the phase-space distribution already signals that this limit is delicate: $f(E)$ depends on $\frac{1}{\Gamma(n-3/2)}$ and since $\Gamma(x) \simeq 1/x$ for $x \to 0^+$

$$\frac{1}{\Gamma\left(n-\frac{3}{2}\right)} \simeq n - \frac{3}{2} = \frac{\gamma}{2-\gamma} \xrightarrow[\gamma\to 0]{} 0\,. \tag{3.33}$$

We notice how the amplitude of the divergence of the distribution vanishes linearly with γ. From the formula of $\gamma_{\rm sp}$ of eq. (3.31) it seems that $\gamma_{\rm sp} \to 9/4$, but the population of cold particles responsible for that slope disappears in the limit. In the following section we properly discuss this case.

3.2.4 Cored halos and the case $\gamma = 0$

We now recover the general family of eq. (3.13) in order to make some considerations on cored halos, which is the case of $\gamma = 0$. We will see how this general treatment also reproduces the Gondolo–Silk result, with the appropriate choice of parameters.

In the following we derive n for $1 \le \alpha \le 2$, but the results for other ranges can be obtained analogously.

In this case we cannot integrate Eddington's formula in closed form, so we study it asymptotically and extract the behavior of $f(E)$ for $E \to 0^+$. In this way we obtain the value of n, which is the only quantity needed in eq. (3.24) to compute the spike slope.

Expanding eq. (3.13) around $r = 0$, we obtain

$$\rho(r) \simeq \rho_s \left(\frac{r}{r_s}\right)^{-\gamma} \left[1 - \frac{\beta-\gamma}{\alpha}\left(\frac{r}{r_s}\right)^{\alpha} + \dots\right]. \tag{3.34}$$

We see that for $\gamma \to 0$ the profile approaches a constant central density, with a leading correction $\propto r^\alpha$.

Inserting this expansion into Eddington's formula, changing the integration variable from ϕ to r and keeping the terms that can produce a divergence, one finds [42]

$$f(E) \sim \int_{r_\star} \frac{dr}{r^3}\, \frac{c_0 + c_1 (r/r_s)^\alpha + c_2 (r/r_s)^{2\alpha} + \dots}{\sqrt{r^{2-\gamma} - E}}, \tag{3.35}$$

where the lower limit $r_\star = E^{1/(2-\gamma)}$ is the radius at which $\phi(r_\star) = E$.

Some care is needed here: the integral of eq. (3.35) is obtained from the small radius expansion of the density, and is therefore not valid over the whole range of integration. However, this is sufficient for our purposes, because we do not need $f(E)$ itself, but only its singular behavior as $E \to 0^+$. Splitting the integral at an arbitrary fixed radius r_1, independent of E, the outer region $r > r_1$ has $r^{2-\gamma} \gg E$: the integrand is a smooth function of the energy there, and this piece approaches a finite constant as $E \to 0^+$, contributing only to the regular part of $f(E)$. Therefore, all the singular behavior comes from the inner region $r_\star \leq r \leq r_1$, where the expansion is valid and where the energy enters only through the lower limit $r_\star \to 0$. For this reason the upper limit of integration is irrelevant for the scaling.

In our particular case of $1 \leq \alpha \leq 2$, the first two coefficients are (up to a constant)

$$\begin{aligned} c_0 &= -2\gamma(3-\gamma), \\ c_1 &= (\alpha-2)(3-\gamma)(\beta-\gamma)\,\frac{(2\alpha-\gamma)(3-\gamma)+\alpha(\alpha-\gamma)}{\alpha(3+\alpha-\gamma)}. \end{aligned} \tag{3.36}$$

Rescaling $r = r_\star x$, a term $\propto r^k$ in the numerator of eq. (3.35) contributes as

$$f(E) \sim E^{-n_k}, \qquad n_k = \frac{6-\gamma-2k}{2(2-\gamma)}, \tag{3.37}$$

provided $n_k > 0$, otherwise the integral is dominated by large radii, the term gives no divergence and only contributes to the regular part of $f(E)$. Note that n_k decreases with k: once a term of the expansion is regular, so are all the subsequent ones. The explicit calculation, together with the analysis of the two endpoints of integration, is reported in appendix B.7. In conclusion, the behavior of $f(E)$ near $E = 0$ is determined by the lowest power k with a non-vanishing coefficient, provided it satisfies $n_k > 0$, which fixes n and, through eq. (3.24), the slope of the spike. If no term satisfies this condition, $f(E)$ is regular and $n = 0$.

There are three important cases:

- For $\gamma > 0$ and independently of α, $c_0 \neq 0$. In this case the $k = 0$ term dominates and we have

$$n = n_0 = \frac{6-\gamma}{2(2-\gamma)}, \qquad \gamma_{\text{sp}} = \frac{9-2\gamma}{4-\gamma}, \tag{3.38}$$

  recovering the result of [44] and Gondolo–Silk.

- For $\gamma = 0$ and for $1 \leq \alpha < 2$, the first term c_0 vanishes and the leading term is the second one, which has $k = \alpha$:

$$n = \frac{3-\alpha}{2}, \qquad \gamma_{\text{sp}} = \frac{3}{2} + \frac{n}{2} = \frac{9-\alpha}{4}. \tag{3.39}$$

  Hence we notice how for a cored halo the spike is milder, $7/4 < \gamma_{\text{sp}} \leq 2$, and its slope is controlled by α, not by γ.

- For $\gamma = 0$ and $\alpha = 2$ both c_0 and c_1 vanish, the distribution function is non-singular ($n = 0$) and the density profile after the adiabatic growth of the black hole has a slope $\gamma_{\text{sp}} = 3/2$. This is the case of the non-singular isothermal profile of eq. (3.42).

We can make some considerations about the result we derived previously: the slope of the spike is a property of the DM profile very close to the black hole, at $r \ll R_{\text{sp}}$, and yet from eq. (3.31) and eq. (3.39) we observe a dependence of γ_{sp} on γ and α, which at first sight look like parameters describing the halo very far away: after the growth of the BH, the initial profile inside $R_{\rm sp}$ no longer exists, having been replaced by the spike itself, while γ is the slope measured on the halo well outside the spike and α describes the transition of the profile around the scale radius r_s, which is orders of magnitude further out.

This is, however, only an apparent paradox. In the Zhao family of eq. (3.13) the parameter α plays two distinct roles: it sets the sharpness of the transition between the two power laws at $r \sim r_s$, but it is also the exponent of the leading correction to the inner power law as $r \to 0$, as we can see in eq. (3.34). It is exclusively through this second role that α enters our calculation: via the coefficient c_1 of eq. (3.36) and the behavior of Eddington's integral at $r_\star \to 0$. The same holds for γ, which is by definition the exponent of the leading term of the same expansion. The spike therefore never probes the halo at large radii: it only probes the way in which the density approaches its central value, and any profile sharing the same $r \to 0$ expansion would give the same $\gamma_{\rm sp}$, however different its behavior at $r \gtrsim r_s$. What is really assumed, when $\gamma_{\rm sp}$ is quoted in terms of (α, γ), is that the fitted profile can be extrapolated all the way down to $r \to 0$.

The mechanism behind this can be traced back to the derivation of the spike.

First, the spike is formed by the initially most bound, hence coldest, particles and the relation between the initial and final energy of eq. (3.20) connects the region $r \ll R_{\rm sp}$ to the initial orbits with $E \to 0^+$. The point is that the parameter n measures how many such particles the initial halo contains.

Second, n is not fixed by the central density $\rho(0)$, nor by the slope of the profile at any observable radius, but is fixed by the leading non-constant term in the expansion of $\rho(r)$ as $r \to 0$, as we show in appendix B.7 from the analysis of Eddington's expansion. Ref. [42] presents an instructive example of what we have just discussed: the profiles $\rho \propto (a+r)^{-2}$ and $\rho \propto (a^2+r^2)^{-1}$, where a is a constant, both approach a constant density at the origin and both fall off as r^{-2} for $r \gg a$, and yet the first has $(\alpha, \beta, \gamma) = (1, 2, 0)$, hence $\gamma_{\rm sp} = 2$, while the second has $\alpha = 2$, hence $\gamma_{\rm sp} = 3/2$. The general criterion [44] is the analyticity of the density at the origin: if ρ can be expanded in even powers of r, i.e. it is an analytic function, the phase-space distribution is regular and the spike has the minimal slope $3/2$; any non-analytic behavior, either a cusp $r^{-\gamma}$ or a correction r^α with $\alpha < 2$, produces a phase-space singularity and a steeper spike.

3.2.5 Annihilation saturation

We also need to consider the DM annihilation at small radii. The growth of the DM density cannot continue indefinitely: in the inner regions of the spike annihilations are so efficient that they set a maximal density, called saturation density

$$\rho_{\rm core} = \frac{m_{\rm DM}}{\langle \sigma v \rangle \, t_{\rm BH}}, \tag{3.40}$$

where $m_{\rm DM}$ is the DM mass, $\langle \sigma v \rangle$ is the cross section and $t_{\rm BH}$ is the age of the black hole, conservatively 10^{10} yr. The explicit derivation is reported in appendix C. The final spike profile can be written as

$$\rho_{\rm spike}(r) = \frac{\rho'(r)\, \rho_{\rm core}}{\rho'(r) + \rho_{\rm core}}, \tag{3.41}$$

which behaves like $\rho'(r)$ where $\rho'(r) \ll \rho_{\rm core}$ and flattens to $\rho_{\rm core}$ where $\rho'(r) \gg \rho_{\rm core}$. The transition happens at the saturation radius $R_{\rm core}$, defined by the condition $\rho'(R_{\rm core}) =$

$\rho_{\rm core}$, i.e. the radius at which the unsaturated spike reaches the saturation density.

Note that flattening eq. (3.41) to a constant $\rho_{\rm core}$ is not the only possible approach: Ref. [46] shows that, since particles on eccentric orbits cross the annihilation-dominated region only briefly, the density inside the saturation radius still has a residual cusp. Our choice is therefore more conservative.

Examples of spike density profiles are shown in fig. 3.1: for the halo we adopt the single power law of eq. (3.7), with different values of γ ranging from 0.01 to 1.3. As a representative cored halo we employ the non-singular isothermal profile [27], which corresponds to the general family of eq. (3.13) with $(\alpha, \beta, \gamma) = (2, 2, 0)$, whose functional form reads

$$\rho_{\rm iso}(r) = \frac{\rho_s}{1 + \left(\dfrac{r}{r_s}\right)^2}\,, \tag{3.42}$$

with $r_s = 1$ kpc. This profile flattens to the constant value ρ_s for $r \ll r_s$ and falls off as r^{-2} at large radii, reproducing flat rotation curves. As discussed in section 3.2.4, this is the case of $\gamma = 0$ and $\alpha = 2$, therefore the spike develops the minimal slope $\gamma_{\rm sp} = 3/2$.

We neglect the cases of higher values of γ since they are not supported even by the most optimistic simulations.

The saturation density is fixed to the representative value $\rho_{\rm core} \simeq 1.4 \times 10^{11}$ GeV/cm^3, corresponding to $m_{\rm DM} = 1$ TeV and $\langle \sigma v \rangle = 2.2 \times 10^{-26}$ cm^3/s.

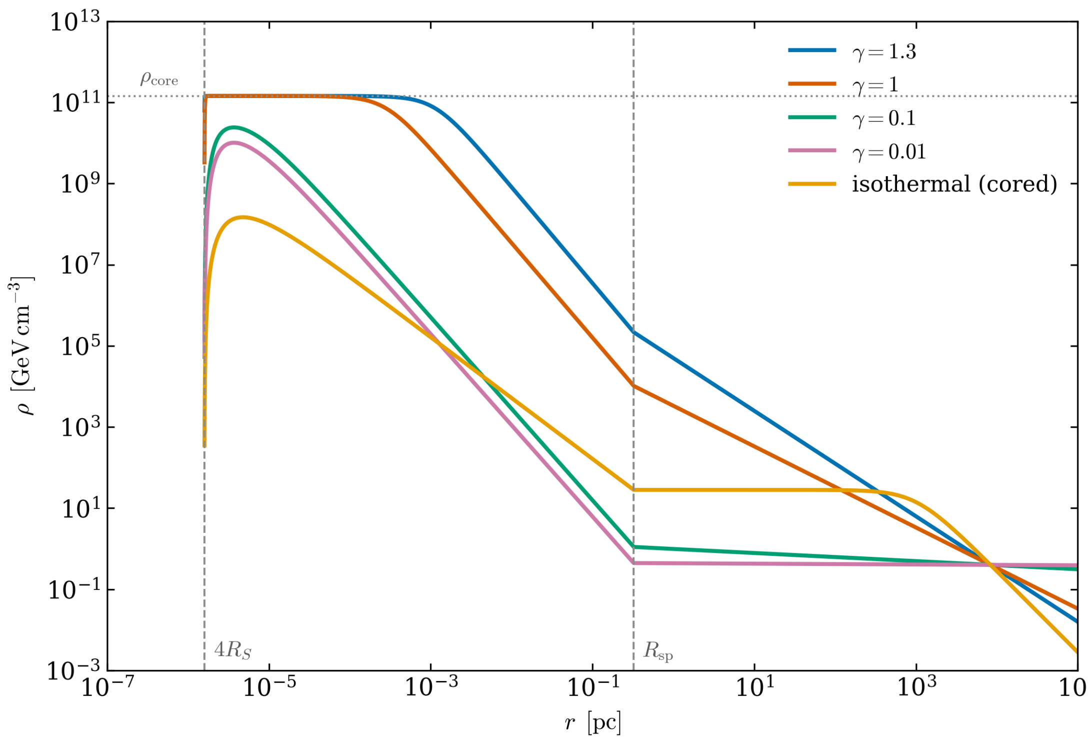

Figure 3.1: *Examples of spike density profiles for different values of the halo inner slope γ: 1.3, 1, 0.1, 0.01, and for an isothermal profile with a flat core of radius 1 kpc, following [40]. The halo profiles are normalized to $\rho_\odot = 0.4$ GeV/cm^3 at $r_\odot = 8.33$ kpc. Both axes use a logarithmic scale to display the wide dynamic range of the profiles, from the region close to the black hole to the outer halo.*

3.3 Benchmark spike profiles

In this section we combine the results obtained previously to build two benchmark spiked profiles, the *Gondolo–Silk* and the *less-stellar-heating* benchmarks, each constructed on both a peaked NFW halo and a cored halo.

We know that the knowledge of the DM density profile in the spike is affected by severe uncertainties, it is therefore desirable to know how the strength of the signals depends on a meaningful parametrisation of these astrophysical uncertainties.

We distinguish two main sources of uncertainty: the poor knowledge of $\rho_{\rm DM}$ in the inner kpc of the Milky Way and the impact of baryonic matter, such as stars, on the DM in the vicinity of Sgr A*. However, these uncertainties are being reduced as our comprehension of the baryonic matter in the region surrounding Sgr A* continues to improve: dramatic observational progress has recently been achieved, for example, on the orbits of stars closest to Sgr A* [47, 48] and on the nuclear star cluster profile [49, 50, 51]. Many of these observational results were unknown at the time of the first studies that aimed to determine $\rho_{\rm spike}$, such as [42], and novel determinations have subsequently been possible, see e.g. [52].

Given these uncertainties, we employ the following general parametrisation of the DM mass density of the MW

$$\rho(r) = \begin{cases} 0 & r < 4R_S, \\ \rho_{\rm spike}(r) & 4R_S \leq r < R_{\rm sp}, \\ \rho_{\rm halo}(r) & r \geq R_{\rm sp}, \end{cases} \tag{3.43}$$

where r is the distance from Sgr A*, which we assume to be at the exact center of the MW, $\rho_{\rm halo}$ is the outer halo density and $\rho_{\rm spike}(r)$ is the saturated spike profile of eq. (3.41).

Since the spike slope is strongly dependent on the halo profile close to the BH, it is crucial to account for the uncertainties in the DM halo distribution at small radii. In what follows we will employ a peaked NFW and a cored profile, defined following [53].

We recall the NFW profile

$$\rho^{\rm NFW}_{\rm halo}(r) = \frac{\rho_s}{\dfrac{r}{r_s}\left(1+\dfrac{r}{r_s}\right)^2}, \tag{3.44}$$

with scale radius r_s and normalization fixed by the local DM density through

$$\rho_s = \rho_\odot \left(\frac{r_\odot}{r_s}\right)\left(1+\frac{r_\odot}{r_s}\right)^2, \tag{3.45}$$

where $r_\odot = 8.33\,$kpc is the distance of the Sun from the Galactic Center. For $\rho_\odot$ we use the same value adopted for the J-factors of table 2.1, which is $\rho(r_\odot) = 0.4$ GeV/cm^3. The scale radius r_s is fixed, as in table 2.1, by the enclosed-mass condition $M(< 60$ kpc$) = 4.7 \times 10^{11}\, M_\odot$, which for the NFW profile gives $r_s \simeq 14.0$ kpc.

For the cored profile we employ the following parametrisation

$$\rho^{\rm cored}_{\rm halo}(r) = \begin{cases} \rho^{\rm NFW}_{\rm halo}(r_c)\left(\dfrac{r}{r_c}\right)^{-\gamma_c} & r < r_c, \\ \rho^{\rm NFW}_{\rm halo}(r) & r \geq r_c, \end{cases} \tag{3.46}$$

where r_c is the radius of the core and $0 \leq \gamma_c < 1$ its inner slope. For MW-sized galaxies, simulations allow for core radii of the order of a kpc, so we assume $r_c = 1$ kpc. Since baryons largely dominate the gravitational potential at those scales, in eq. (3.46) we can safely use the same values of ρ_s and r_s obtained for the NFW profile in eq. (3.44). For the slope we adopt $\gamma_c = 0.4$, a representative value of the peak softening found below 1 kpc by recent FIRE simulations including both baryons and DM [54]. Note that for $\gamma_c = 0$ we recover the cored NFW profile of eq. (2.3), which is a conservative choice since the density inside r_c is constant. Strictly speaking, for $\gamma_c > 0$ this profile is not truly cored, but only softened with respect to NFW, we will nevertheless refer to it as cored for brevity.

It is important to note that the spike does not extend over the whole region of influence of the black hole: it begins to grow around the radius $R_{\rm sp} \simeq 0.2\, R_h$, where

$$R_h = \frac{GM_{\rm BH}}{v_0^2} \tag{3.47}$$

is the gravitational influence radius of the BH, defined by the condition that the potential energy due to the BH equals the typical kinetic energy of a DM particle in the halo. Here v_0 is the velocity dispersion of the DM particles in the inner halo, which we estimate from the velocity dispersion of the stars in the same region, since DM and stars move in the same gravitational potential. The numerical factor 0.2 is the result of simulations of the adiabatic growth of the black hole [55].

Adopting $M_{\rm BH} \simeq 4.15 \times 10^6\, M_\odot$ for Sgr A* [39] and $v_0 \simeq 105$ km s^{-1} [53], one finds

$$R_h \simeq 1.6 \text{ pc}, \qquad R_{\rm sp} \simeq 0.32 \text{ pc}. \tag{3.48}$$

Note that this estimate of $R_{\rm sp}$ differs substantially from the one of eq. (3.32), obtained by Gondolo and Silk from the condition that the halo mass enclosed within $R_{\rm sp}$ be comparable to $M_{\rm BH}$, which for the NFW profile of eq. (3.44) is met more than an order of magnitude further out. The two conditions would be equivalent for a self-gravitating halo, where $v^2 \sim GM_{\rm halo}(<r)/r$ and $M_{\rm halo}(<R) = M_{\rm BH}$ is the same requirement as $R = GM_{\rm BH}/v^2$. They differ here because the potential of the inner Galaxy is dominated by the baryons: the mass criterion ignores them altogether, while v_0, inferred from the stars, is several times larger than the DM mass alone would produce, and $R_h \propto v_0^{-2}$. Both criteria identify the scale at which the black hole starts to dominate the potential, and here we adopt eq. (3.48) for consistency with Ref. [53]; it is also the conservative choice, since the spike density grows with $R_{\rm sp}$. We return to this assumption in section 3.3.3.

3.3.1 Gondolo–Silk benchmark

From eq. (3.31), for an NFW profile, which has $\gamma = 1$, one obtains a spike slope of $\gamma_{\rm sp} = 7/3$, while for the cored halo, which has $\gamma = \gamma_c = 0.4$, one obtains $\gamma_{\rm sp} \simeq 2.28$. Now, neglecting the factor $g_\gamma(r)$, which is replaced by the parametrisation that we adopted, we obtain the Gondolo–Silk (GS) profile

$$\rho'_{\rm GS}(r) = \rho_{\rm halo}(R_{\rm sp}) \left(\frac{r}{R_{\rm sp}}\right)^{-\gamma_{\rm sp}}, \qquad 4R_S \leq r < R_{\rm sp}, \tag{3.49}$$

where $\rho_{\rm halo}$ is the NFW profile of eq. (3.44) or the cored profile of eq. (3.46), with the corresponding value of $\gamma_{\rm sp}$.

As discussed in section 3.2.4, the case $\gamma_c = 0$ is subtle: the halo has a flat core, so the spike slope is $\gamma_{\rm sp} = 3/2$ and not the value $9/4$ suggested by the naive limit $\gamma \to 0^+$ of eq. (3.31).

3.3.2 Less-stellar-heating benchmark

Now we consider the gravitational effect of the baryons surrounding Sgr A*: this interaction between DM and the baryons dampens the spike. The DM spike may be significantly softened due to gravitational heating by the nuclear star cluster, i.e. the stars within the inner few pc of the MW. Gnedin and Primack in [56] obtained an equilibrium spike solution of

$$\gamma_{\rm sp}^{\rm heated} = 1.5. \tag{3.50}$$

We refer to this case as the *stellar-heating* benchmark. Instead, in the *less-stellar-heating* (LSH) benchmark, since there are only a few older/brighter giants in the inner region, there should be no scattering between DM and stars in $r < 0.01$ pc, hence the DM spike should theoretically not be softened within this region and follow the Gondolo–Silk slope of the corresponding halo. Imposing continuity at $r_b = 0.01$ pc, the unsaturated spike reads

$$\rho'_{\rm LSH}(r) = \begin{cases} \rho_{\rm halo}(R_{\rm sp}) \left(\dfrac{r_b}{R_{\rm sp}}\right)^{-3/2} \left(\dfrac{r}{r_b}\right)^{-\gamma_{\rm sp}}, & 4R_S \leq r < r_b, \\ \rho_{\rm halo}(R_{\rm sp}) \left(\dfrac{r}{R_{\rm sp}}\right)^{-3/2}, & r_b \leq r < R_{\rm sp}, \end{cases} \tag{3.51}$$

where again $\rho_{\rm halo}$ denotes either the NFW or the cored halo, with $\gamma_{\rm sp} = 7/3$ and $\gamma_{\rm sp} \simeq 2.28$ respectively.

3.3.3 Limitations of the benchmarks

The benchmarks defined above encompass many of the uncertainties affecting the determination of spike profiles. However, there are other sources of uncertainty that they do not account for.

First, we have not considered halo profiles steeper than NFW, although recent simulations do produce them. The correspondingly steeper spikes would yield larger J-factors and hence a larger predicted γ-ray flux, improving the sensitivity of indirect searches for DM annihilation towards the Galactic Center.

Second, we determine the spike radius $R_{\rm sp}$ through the velocity dispersion of the stars, implicitly assuming that DM and baryons are in kinetic equilibrium. This holds in the less-stellar-heating benchmark, but could perhaps be too conservative for GS, where we neglect DM heating by stars and so DM could have a smaller velocity dispersion, leading to a larger spike radius. Since the GS benchmark provides the strongest constraints anyway, we use the same $R_{\rm sp}$ for both benchmarks.

Third, if the GC underwent mergers with other galaxies, then the shape of the spike would be affected. However, the Milky Way is unlikely to have undergone a major merger in its recent past: Gaia data suggest that the last one, the so-called Gaia-Enceladus/Sausage event, took place several billion years ago [57, 58, 59], so the spike has had time to regenerate. Therefore, we do not account for major merger effects in our benchmarks.

Finally, we assumed that Sgr A* has been sitting within tens of pc of the center of the halo density distribution throughout most of its formation history. This assumption is supported by the measured slope of the density of the nuclear star cluster, see e.g. [51], and by the fact that the gravitational dynamics is by far dominated by baryons. If this were not the case, the resulting spike would be softened.

3.4 J-factors of spiked profiles

For both benchmarks, the final profile $\rho_{\mathrm{spike}}(r)$ is obtained by applying the annihilation saturation of eq. (3.41) to $\rho'(r)$.

We can now compute their J-factors in order to quantify the enhancement of the annihilation signal produced by the spike.

In section 2.1 we integrated the J-factors over a region with a mask on the latitude $|b| < 0.3^\circ$ to remove the photon background from the galactic ridge. Now we cannot integrate over the same region since the spike extends only up to $R_{\mathrm{sp}} \simeq 0.32$ pc, while the mask excludes all the l.o.s. passing within $\simeq 44$ pc of the GC, therefore the spiked profiles would give exactly the same J-factors as the corresponding halo alone. For this reason we have to define a different region of integration. The key point is that the spike subtends an angle of only $\simeq 0.002^\circ$ and, specifically for the NFW profile, its signal dominates over that of the surrounding halo: as long as the region of integration contains the spike, the resulting J-factors depend only mildly on its exact shape and size. Therefore, following Ref. [53], we integrate over the central $0.1^\circ \times 0.1^\circ$ pixel centered on Sgr A*, so that our J-factors are directly comparable to theirs. As a consequence, from now on we no longer use the H.E.S.S. Inner Galaxy Survey limits of section 2.1 [2], which mask the $|b| < 0.3^\circ$ region, but the limits derived in Ref. [53] over this central pixel. These, in turn, are obtained from the H.E.S.S. observations of the Galactic Center [60], a measurement of the very-high-energy γ-ray flux from the central source associated with Sgr A*, reinterpreted as an upper limit on a possible DM annihilation contribution.

All the other parameters are the same used for table 2.1: the local density $\rho_\odot = 0.4$ GeV/cm^3 at $r_\odot = 8.33$ kpc and, for the NFW halo, the scale radius $r_s \simeq 14.0$ kpc fixed by the enclosed-mass condition $M(< 60 \text{ kpc}) = 4.7 \times 10^{11}\, M_\odot$. The spike parameters are those of eq. (3.48), with the density set to zero below $4R_S$ according to eq. (3.43).

Another key consideration is the choice of the annihilation cross section $\langle \sigma v \rangle$. From eq. (3.40) it is clear that a bigger cross section corresponds to a smaller saturation density. In the following, we calculate the J-factors in the non-annihilating limit $\langle \sigma v \rangle \to 0$, where the saturation density diverges and therefore the J-factors are the maximal ones, and for a representative value of $\langle \sigma v \rangle = 2.2 \times 10^{-26}$ cm^3/s and $m_{\mathrm{DM}} = 1$ TeV, corresponding to $\rho_{\mathrm{core}} \simeq 1.4 \times 10^{11}$ GeV/cm^3. In the latter case it is important to notice that the saturated J-factor is no longer a purely astrophysical quantity, and the expected flux is not linear in $\langle \sigma v \rangle$ [53].

Since R_{sp} is much smaller than the size of the region of observation, the spike behaves as a point-like source and its contribution can be computed as a volume integral

$$J_{\mathrm{sp}} = \frac{1}{r_\odot^2} \int_{4R_S}^{R_{\mathrm{sp}}} 4\pi r^2\, \rho_{\mathrm{spike}}^2(r)\, dr, \tag{3.52}$$

to be added to the line-of-sight integral of the corresponding halo over the pixel. Note that in the non-annihilating limit $\rho_{\mathrm{spike}}(r) \to \rho'(r)$. The results are reported in table 3.1.

$\log_{10}(J_{0.1^\circ\times0.1^\circ}\,[\mathrm{GeV}^2/\mathrm{cm}^5])$	NFW	NFW + GS	NFW + LSH	Core	Core + GS	Core + LSH
$\langle\sigma v\rangle \to 0$	20.70	27.74	25.22	18.63	22.87	20.53
$\langle\sigma v\rangle = 2.2\times10^{-26}\ \mathrm{cm}^3/\mathrm{s}$	20.70	23.62	22.02	18.63	20.60	19.19

Table 3.1: *J-factors integrated over the central* $0.1^\circ \times 0.1^\circ$ *pixel centered on Sgr A*, following Ref. [53], for the NFW and cored* ($\gamma_c = 0.4$ *and* $r_c = 1$ *kpc) halos, alone and with the two benchmark spike profiles GS and LSH. The J-factors are calculated in the non-annihilating limit* $\langle\sigma v\rangle \to 0$ *(top row) and with the saturation of eq.* (3.41) *for* $m_{\mathrm{DM}} = 1$ *TeV and* $\langle\sigma v\rangle = 2.2\times10^{-26}\ \mathrm{cm}^3/\mathrm{s}$ *(bottom row).*

In fig. 3.2 we plot the density profiles for both halos, alone and with the two spike benchmarks. The spikes are shown unsaturated, as in the non-annihilating limit $\langle\sigma v\rangle \to 0$, nevertheless the horizontal dotted line indicates the saturation density ρ_{core}.

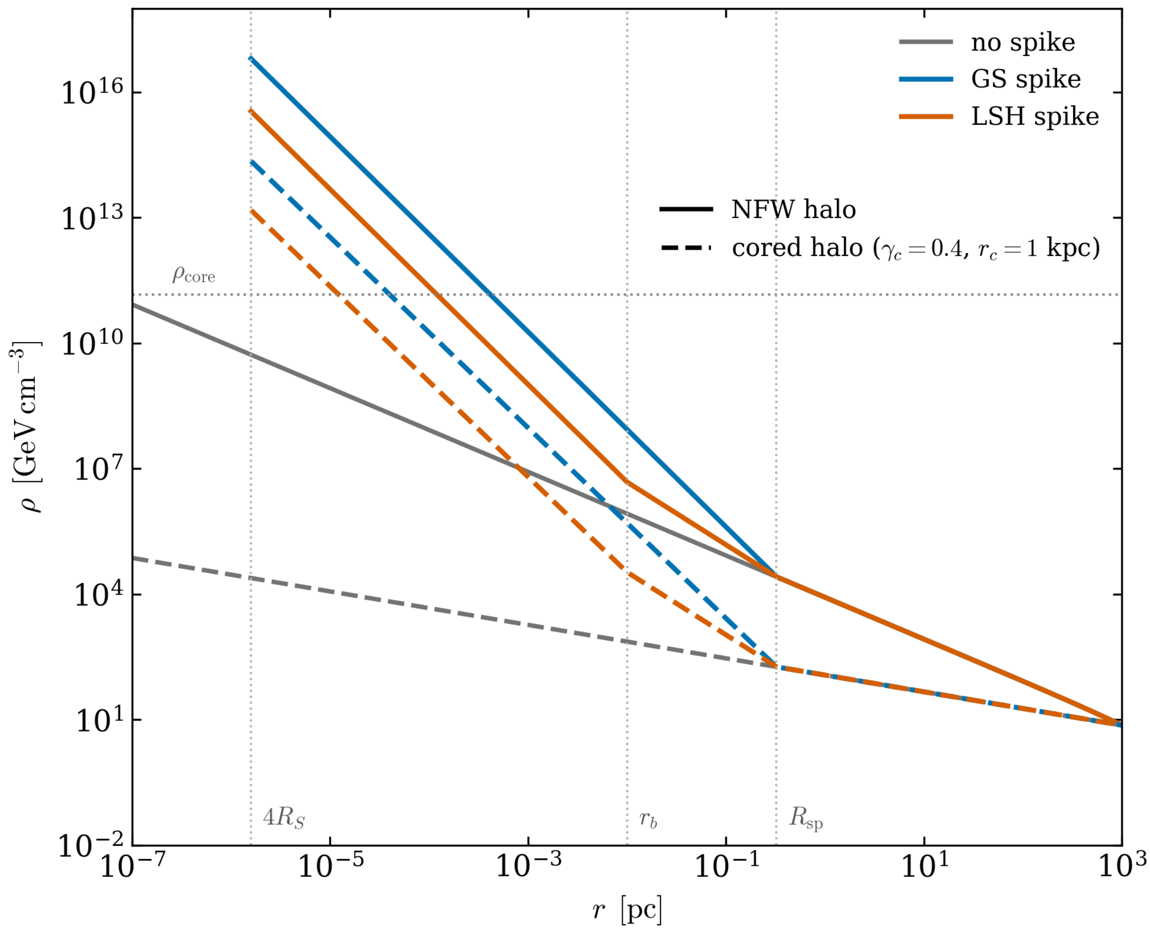

Figure 3.2: *DM density profiles as a function of the distance from Sgr A*, alone and with the two spike benchmarks GS and LSH. Solid lines refer to the NFW halo and dashed lines to the cored halo with* $\gamma_c = 0.4$ *and* $r_c = 1$ *kpc; curves of the same color correspond to the same case (no spike, GS or LSH spike), so that the comparison between the two halos is immediate. The spikes are shown unsaturated, i.e. in the non-annihilating limit* $\langle\sigma v\rangle \to 0$.

The results obtained meet the expectations, and are evident in both table 3.1 and fig. 3.2: we observe a huge enhancement for the NFW halo, up to about seven orders of magnitude, and a much milder one for the cored halo. In both cases, the GS benchmark produces a stronger enhancement than the LSH and the J-factors in the non-annihilating limit are larger than the ones where the saturation is included. The values for the halos alone are the same in both cases, since their densities stay below ρ_{core} at all radii above $4R_S$.

It is crucial to compare the two sources of uncertainty discussed previously: we note that the same spike benchmark yields J-factors that differ up to almost five orders of magnitude between the two halos, while on the same halo profile, the difference between the two benchmarks is about two orders of magnitude. The uncertainty on the inner halo profile therefore dominates over the uncertainty on the spike shape.

3.5 Impact of the spike on the cross section limits

The enhancement of the J-factors produced by the spike translates directly into stronger constraints on the DM annihilation cross section. Therefore, in this section we repeat the comparison of fig. 2.1 between the experimental upper limits and the thermal relic cross section of our model, this time including the benchmark spikes of section 3.3.

Ref. [53] provides 95% C.L. upper limits on $\langle\sigma v\rangle$ in the W^+W^- channel, derived from the H.E.S.S. observations [60] of the central $0.1^\circ \times 0.1^\circ$ pixel centered on Sgr A*, assuming an NFW halo with the GS and LSH spikes. The limits are provided for DM masses $m_{\text{DM}} \gtrsim 0.3$ TeV.

As done in the previous chapter, we adapt these limits to our halo parameters. Ref. [53] adopts $\rho_\odot = 0.383$ GeV/cm^3 at $r_\odot = 8.2$ kpc, $r_s = 18.6$ kpc and $M_{\text{BH}} = 4.3 \times 10^6\, M_\odot$, and we rescale the limits with the ratio of the J-factors computed for the two sets of parameters over the same region of observation. We use the saturated J-factors of table 3.1, i.e. those obtained for $m_{\text{DM}} = 1$ TeV and $\langle\sigma v\rangle = 2.2 \times 10^{-26}$ cm^3/s. We obtain $J^{\text{ref}}/J^{\text{our}} \simeq 0.78$ for the GS benchmark and $\simeq 0.75$ for the LSH one.

Note that for spiked profiles the limits are not exactly proportional to $1/J$, since the saturation density ρ_{core}, and hence the J-factor itself, depends on m_{DM} and $\langle\sigma v\rangle$ [53]. The rescaling is therefore an approximation, which we expect to be adequate here since our halo parameters differ only mildly from those of Ref. [53].

The resulting limits are shown in fig. 3.3, together with the no-spike NFW limit from fig. 2.1 and the thermal relic cross section of our model. All the curves in fig. 3.3 refer to the peaked NFW halo of eq. (3.44), combined with the GS and LSH spikes of section 3.3.

It is important to underline that the no-spike NFW limit and the spiked ones are derived over different observation regions: the Inner Galaxy Survey [2] ($0.5^\circ < \theta < 3^\circ$) for the former, and the central $0.1^\circ \times 0.1^\circ$ pixel for the latter. This choice reflects the different nature of each signal: the NFW halo produces a diffuse annihilation flux, therefore is best constrained over a wide region, whereas the spike is an essentially point-like source at Sgr A*, whose signal is optimally isolated from the astrophysical background by the smallest region that still contains it.

We immediately notice the dramatic impact of the GS spike: the limit reaches a minimum of $\simeq 1.2 \times 10^{-31}$ cm^3/s at $m_{\text{DM}} \sim 20$ TeV, more than five orders of magnitude below the minimum of the no-spike limit, $\simeq 5 \times 10^{-26}$ cm^3/s at $m_{\text{DM}} \simeq 1.6$ TeV. Such low values of cross section are made accessible by the saturation: it follows from eq. (3.40) that a smaller $\langle\sigma v\rangle$ implies a larger saturation density and hence a larger J-factor, so the expected flux from the saturated region does not simply decrease with the cross section. This is the same effect we already discussed when we questioned the validity of the rescaling.

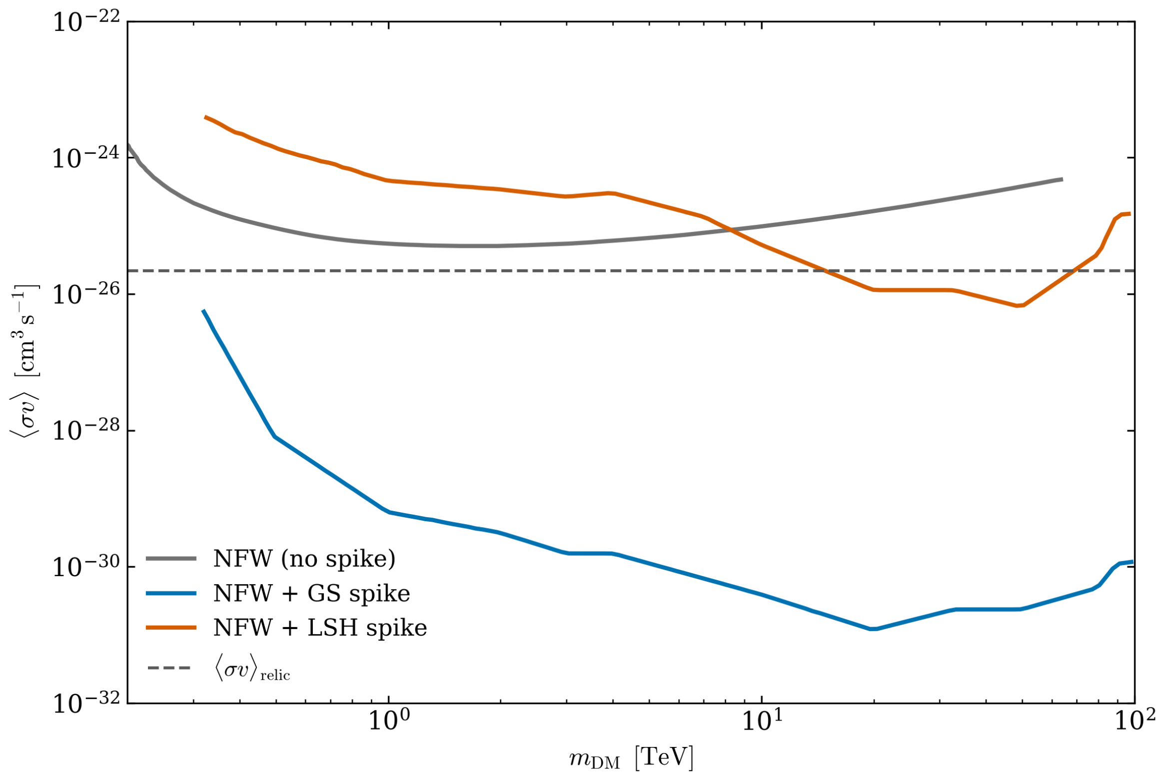

Figure 3.3: *Our result for the 95% C.L. upper limits on the annihilation cross section in the* W^+W^- *channel, rescaled to our halo parameters, for the peaked NFW halo of eq.* (3.44). *The blue (NFW + GS spike) and orange (NFW + LSH spike) curves are obtained from the limits of Ref. [53], derived from the H.E.S.S. observations of the Galactic Center [60], they correspond respectively to the Gondolo–Silk spike of eq.* (3.49) *and to the less-stellar-heating spike of eq.* (3.51)*, both defined in section 3.3. The grey NFW curve without spike is the one of fig. 2.1, based on the H.E.S.S. Inner Galaxy Survey [2]. The dashed line is the cross section that reproduces the observed relic abundance in our model.*

The GS limit lies below the thermal relic value over the whole mass range for which the limits are available: already at $m_{\rm DM} \simeq 0.32$ TeV it is a factor $\simeq 4$ below it, and the margin grows to five orders of magnitude around 20 TeV. Our model therefore excludes this benchmark for every $m_{\rm DM}$ between 0.3 and 100 TeV.

The LSH limit is instead much weaker, but it still dips below the thermal relic cross section in a window of high masses: it crosses it at $m_{\rm DM} \simeq 15$ TeV, reaches a minimum of $\simeq 6.7 \times 10^{-27}$ cm^3/s at $m_{\rm DM} \simeq 48$ TeV, a factor $\simeq 3$ below the relic value, and rises back above it at $m_{\rm DM} \simeq 69$ TeV. Thermal relic DM is therefore excluded in the range $15 \lesssim m_{\rm DM}/\text{TeV} \lesssim 69$ even for this milder spike, and allowed outside it.

These results confirm the interpretation given at the end of the previous chapter: an excluded point expresses the simultaneous incompatibility of the assumed DM distribution, mass and cross section. Since the thermal relic cross section is a robust theoretical prediction, we analyze its compatibility with the DM profile.

We obtain that if thermal DM with $0.3 \lesssim m_{\rm DM}/\text{TeV} \lesssim 100$ exists, then the combination of an NFW halo and a GS spike is excluded, meaning that either the inner halo is shallower than NFW, or the spike has been softened by stellar heating, or it never formed. Softening the spike is however not sufficient over the whole mass range: in the window $15 \lesssim m_{\mathrm{DM}}/\mathrm{TeV} \lesssim 69$ even the LSH benchmark on an NFW halo is excluded, so there the inner halo itself must be shallower than NFW, or the spike must be absent altogether.

Observations of the Galactic Center thus probe not only particle DM properties but also the dynamical history of the innermost region of the Milky Way.

Conclusions

In this thesis we studied the impact of the uncertainties on the DM density profile of the Milky Way on the indirect detection constraints obtained from the Galactic Center. We mainly investigated this region since the DM density is expected to rise towards the center, leading to a flux of gamma rays that is orders of magnitude larger than that predicted from the brightest dwarf galaxies. However, the GC is severely affected by the uncertainties on the density profile and by the astrophysical background.

We first compared a set of representative density profiles, namely the Einasto, Burkert and cored NFW profiles, fixing their parameters through observational constraints and computing their J-factors (section 2.1). The latter, integrated over a small region around the Galactic Center, span more than two orders of magnitude between the most peaked profile (Einasto) and the most cored one (Burkert), as summarized in table 2.1. This has severe consequences on the upper bounds on the annihilation cross section. In particular, the upper bound derived under the Burkert assumption is roughly a factor $\sim 4 \times 10^2$ weaker than the one obtained under Einasto. We then considered a simple thermal relic model, in which DM annihilates into a pair of mediators that subsequently decay into W bosons, with the annihilation cross section fixed by the relic abundance to $\langle \sigma v \rangle = 2.2 \times 10^{-26}$ cm^3/s for self-conjugate DM (section 2.2). Comparing this prediction with the H.E.S.S. Inner Galaxy Survey limits [2], provided for the NFW profile and rescaled to our halo parameters, we found that the model is not excluded at any DM mass, neither for the NFW profile nor for the cored one, whose limit was obtained through a further rescaling of the J-factors (fig. 2.1).

Subsequently, we studied the adiabatic growth of the supermassive black hole Sgr A* at the center of the Milky Way (section 3.1): the black hole redistributes the inner DM into a dense cusp, the spike, strongly enhancing the expected annihilation signal (fig. 3.2). We introduced two benchmark spike profiles, the steep Gondolo–Silk (GS) spike (section 3.2.3) and a milder one accounting for stellar heating (LSH, section 3.3.2), and compared them with our thermal relic model (section 3.3). The spike enhances the J-factor of the innermost region by several orders of magnitude (table 3.1), and correspondingly strengthens the cross section limits derived from the H.E.S.S. observations of Sgr A* (section 3.5). For the GS benchmark, thermal relic DM is excluded over the whole mass range probed, $0.3 \lesssim m_{\rm DM}/\text{TeV} \lesssim 100$, while for the LSH benchmark it is excluded only in the window $15 \lesssim m_{\rm DM}/\text{TeV} \lesssim 69$ (fig. 3.3).

These results clearly show that the annihilation cross section constraints depend critically on both the poorly known inner DM distribution and the assumed spike benchmark. Even within the NFW assumption, the choice of the spike benchmark alone moves the excluded region from the entire mass range to a narrow window at high masses. Nevertheless, it should be stressed that the two sources of uncertainty are not independent, since the spike develops from the inner halo and therefore inherits the uncertainties in both its inner slope and density normalization.

Acknowledgements

To my supervisor, Prof. Filippo Sala, who guided me throughout the writing of this thesis. He constantly encouraged me never to take anything for granted, to question what I was studying, and to approach this experience as a challenge. He made me feel continuously motivated to go deeper and to study each concept in greater detail. I believe that this way of approaching my work is one of the most valuable lessons he could have taught me. For all of this, I owe him my sincere thanks.

To my mother, my greatest point of reference, without whom I would not be who and where I am today. Thank you for supporting me in everything I do, and for always doing your very best to shield me from the difficulties and unexpected challenges of everyday life. I am deeply grateful for everything you have done for me, and for the love with which you have always been by my side.

To my sister, with whom, as the years go by, I find myself becoming ever closer. Growing up by her side has shaped much of who I have become. I know that she will always be one of the certainties in my life, someone I can always rely on.

To my father, who, when I was younger, taught me the values that matter in life. I see a great deal of myself in him, and I am grateful for the many passions he has passed on to me.

To my grandparents and my uncle, who have always given me a sense of what family truly means. Whenever I am with them, I feel the love, warmth, and spontaneity that make our relationship so special. They are a fundamental part of my life and of my journey. Their presence has been genuine and unconditional, and it has meant more to me than they know.

To Erea, who has accompanied me every day throughout this journey. She has always known how to support me in moments of difficulty and to share in my happiness whenever I achieved something I had worked for. She has given me so much strength and determination, but above all, she has made me feel that my goals were her goals too. Seeing how genuinely happy she was at those moments made every success feel even more meaningful. I could not have asked for a better person by my side.

To all my friends, with whom, despite the distance, I have maintained, and will always maintain, an unbreakable bond. They have been an important part of my life, and I know that, no matter how far apart we may be, I can count on them.

Appendix A

Gamma ray flux from dark matter annihilation

In this appendix we derive the γ-ray flux from DM annihilation and the associated J-factor introduced in section 1.3.1.

The gamma ray flux produced by DM annihilation can be derived starting from the local DM density distribution. The number of DM pairs contained in a volume d^3r at position $\vec{r}$ is

$$dN = d^3r \frac{1}{2} \left(\frac{\rho_{\rm DM}(\vec{r})}{m_{\rm DM}} \right)^2 , \tag{A.1}$$

where $\rho_{\rm DM}(\vec{r})$ is the DM mass density. We assume self-conjugate DM, i.e. the DM particles coincide with their antiparticles. On the other hand, in the case where DM particles can interact only with their own antiparticles, the factor 1/2 must be replaced by 1/4. There is a quadratic dependence on the density since two DM particles are required for annihilation, whereas in the case of decay the dependence would be linear. We introduce the factor 1/2 to avoid double counting of particle pairs.

Assuming that a pair of DM particles annihilates into a pair of SM particles f, with a cross section $\langle \sigma v \rangle_f$, then multiplying eq. (A.1) by $\langle \sigma v \rangle_f$ and summing over all possible final states, we obtain the number of annihilations per second in the volume d^3r

$$\frac{dN}{dt} = d^3r \frac{1}{2} \left(\frac{\rho_{\rm DM}(\vec{r})}{m_{\rm DM}} \right)^2 \sum_f \langle \sigma v \rangle_f . \tag{A.2}$$

Now multiplying this rate by the number of photons produced per annihilation in the channel f within an infinitesimal energy bin dE, i.e. $\frac{dN_{f\to\gamma}}{dE} dE$, we obtain the number of photons produced per unit time and energy

$$\frac{dN_\gamma}{dtdE} = d^3r \frac{1}{2} \left(\frac{\rho_{\rm DM}(\vec{r})}{m_{\rm DM}} \right)^2 \sum_f \langle \sigma v \rangle_f \frac{dN_{f\to\gamma}}{dE} . \tag{A.3}$$

As we show in fig. A.1, only a fraction of the photons produced at a distance s from the observer reaches the telescope. Since the emission at each point is isotropic, the photons spread over a sphere of area $4\pi s^2$, so a detector of surface $S_{\rm tel}$ collects the geometric fraction

$$\frac{S_{\rm tel}}{4\pi s^2} \tag{A.4}$$

of the total number of photons produced. The solid angle $\Delta\Omega$ and the energy bin ΔE define the angular and spectral acceptance over which the signal is collected, and do not enter as a suppression factor.

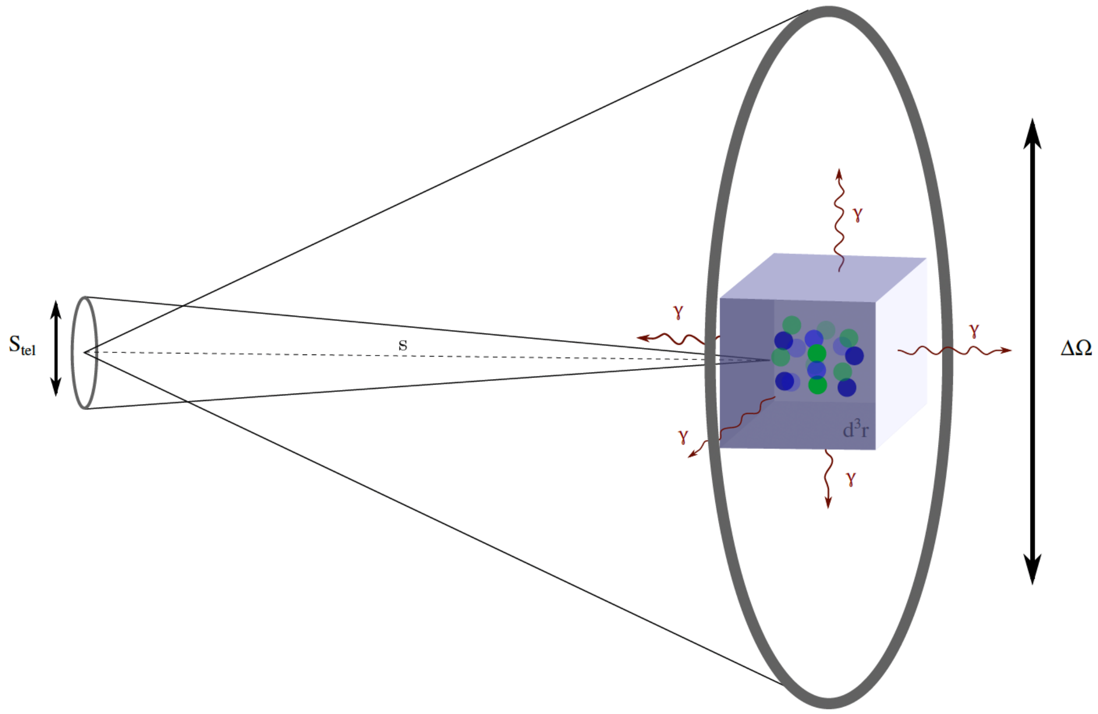

Figure A.1: *A telescope of surface $S_{\rm tel}$ at line-of-sight distance s collects the fraction $\frac{S_{\rm tel}}{4\pi s^2}$ of the photons produced by the isotropic emission [61].*

The photon flux, i.e. the number of photons per unit detector area, time and energy, is obtained by multiplying the emission rate by the fraction eq. (A.4) and dividing by the collecting area $S_{\rm tel}$, which therefore cancels

$$\frac{d\Phi_\gamma}{dE} = \int \frac{1}{4\pi s^2}\, d^3r\, \frac{1}{2}\left(\frac{\rho_{\rm DM}(\vec{r})}{m_{\rm DM}}\right)^2 \sum_f \langle\sigma v\rangle_f \frac{dN_{f\to\gamma}}{dE}. \tag{A.5}$$

Writing the volume element seen by the observer as $d^3r = s^2\, ds\, d\Omega$, with s the coordinate along the line of sight, and integrating over the line of sight we obtain the differential photon flux per unit solid angle and energy

$$\frac{d\Phi_\gamma}{d\Omega dE}(\theta) = \frac{1}{2}\frac{r_\odot}{4\pi}\left(\frac{\rho_\odot}{m_{\rm DM}}\right)^2 J_{\rm ann}(\theta) \sum_f \langle\sigma v\rangle_f \frac{dN_{f\to\gamma}}{dE}, \tag{A.6}$$

where in the particular case of the Milky Way

$$J_{\rm ann}(\theta) = \int_{l.o.s} \frac{ds}{r_\odot}\left(\frac{\rho_{\rm DM}(r(s,\theta))}{\rho_\odot}\right)^2 \tag{A.7}$$

is the annihilation J-factor. Here s is the distance from the observer along the line of sight, θ is the angle between the line of sight and the direction of the Galactic Center, and r is the galactocentric radius, i.e. the distance from the Galactic Center that sets the DM density

$\rho_{\rm DM}(r)$; it is related to s and θ by $r = \sqrt{r_\odot^2 + s^2 - 2\,r_\odot\,s\cos\theta}\,$. Finally, $r_\odot \simeq 8.33$ kpc is the distance from the Earth to the Galactic Center and $\rho_\odot \simeq 0.4$ GeV/cm^3 is the local DM mass density.

Note that a similar treatment for DM decay leads to

$$\frac{d\Phi_\gamma}{d\Omega\,dE}(\theta) = \frac{r_\odot}{4\pi}\left(\frac{\rho_\odot}{m_{\rm DM}}\right) J_{\rm dec}(\theta) \sum_f \Gamma_f\,\frac{dN_{f\to\gamma}}{dE}\,, \tag{A.8}$$

where

$$J_{\rm dec}(\theta) = \int_{l.o.s} \frac{ds}{r_\odot}\left(\frac{\rho_{\rm DM}(r(s,\theta))}{\rho_\odot}\right) \tag{A.9}$$

is the J-factor for decay and Γ_f is the decay rate in the channel f. As expected, we obtain a linear dependence on the DM density.

Appendix B

Phase-space calculations for the adiabatic spike

In this appendix we report all the explicit derivations used in the study of the DM spike in chapter 3.

B.1 The density as an integral over energy and angular momentum

Here we derive eq. (3.2) of section 3.1.

In a spherically symmetric system it is useful to decompose the velocity into its radial v_r and tangential v_t components. In cylindrical coordinates, recalling once more the invariance of f under rotations, the volume element is $d^3v = 2\pi\, v_t\, dv_t\, dv_r$, where we already integrated over the azimuthal angle. The density becomes

$$\rho'(r) = \int f'\, d^3v = 2\pi \int f'\, v_t\, dv_t\, dv_r. \tag{B.1}$$

We now change variables again from (v_r, v_t) to (E', L'), defined by

$$E' = \phi'(r) + \frac{v_r^2 + v_t^2}{2}, \qquad L' = r\, v_t, \tag{B.2}$$

where ϕ' is the gravitational potential and the primes indicate that these quantities are evaluated after the formation of the black hole.

At fixed r, the Jacobian is

$$\frac{\partial(E', L')}{\partial(v_r, v_t)} = \det \begin{pmatrix} v_r & v_t \\ 0 & r \end{pmatrix} = r\, v_r \qquad \Longrightarrow \qquad dv_r\, dv_t = \frac{dE'\, dL'}{r\, v_r}. \tag{B.3}$$

Now we notice that this change of coordinates is not injective: to a given (E', L') there correspond two velocities: the orbit crosses the radius r once moving outward ($v_r > 0$) and once moving inward ($v_r < 0$), with the same $|v_r|$. Hence we have to account for both by multiplying the integral by a factor of two

$$\rho'(r) = 2 \times 2\pi \int \frac{L'}{r} \frac{dE'\, dL'}{r\, v_r}\, f'(E', L') = \int dE' \int dL' \, \frac{4\pi L'}{r^2 v_r}\, f'(E', L'). \tag{B.4}$$

The integration limits follow from the requirements that the orbit is bound ($E' < 0$), that it is not captured by the BH ($L' > L'_c$), and that $v_r^2 \geq 0$ ($L' < L'_m$).

B.2 Potential of the power-law halo

This derivation completes the potential used in section 3.2.2.

For the density profile

$$\rho(r) = \rho_s \left(\frac{r}{r_s}\right)^{-\gamma}, \qquad 0 \leq \gamma < 2, \tag{B.5}$$

the enclosed mass is

$$M_h(r) = \int_0^r 4\pi r'^2 \rho(r')\, dr' = \frac{4\pi \rho_s r_s^\gamma}{3-\gamma}\, r^{3-\gamma}, \tag{B.6}$$

which converges at the center for $\gamma < 3$.

We now recall Poisson's equation for a spherically symmetric system

$$\nabla^2 \phi = \frac{1}{r^2}\frac{d}{dr}\left(r^2 \frac{d\phi}{dr}\right) = 4\pi G\, \rho(r). \tag{B.7}$$

Integrating this equation we obtain Newton's theorem

$$r^2 \frac{d\phi}{dr} = \int_0^r 4\pi G\, \rho(r')\, r'^2\, dr' = G\, M_h(r) \qquad \Longrightarrow \qquad \frac{d\phi}{dr} = \frac{G\, M_h(r)}{r^2}. \tag{B.8}$$

Now, substituting $M_h(r)$ from eq. (B.6) and integrating once more, with the boundary condition $\phi(0) = 0$, we derive the potential

$$\phi(r) = \frac{4\pi G \rho_s r_s^\gamma}{3-\gamma} \int_0^r r'^{\,1-\gamma}\, dr' = \phi_0 \left(\frac{r}{r_s}\right)^{2-\gamma}, \qquad \phi_0 = \frac{4\pi G \rho_s r_s^2}{(3-\gamma)(2-\gamma)}. \tag{B.9}$$

Note that the last integral, $\int_0^r r'^{\,1-\gamma}\, dr' = r^{2-\gamma}/(2-\gamma)$, converges only for $\gamma < 2$. Therefore the condition at the origin $\phi(0) = 0$ is admissible.

Another important consideration is that, although derived here for the single power law, this result has a wider validity: for any spherically symmetric density profile with inner slope γ, the potential has the same central behavior, determined by the enclosed mass.

B.3 Eddington's inversion formula

Here we derive Eddington's formula used in section 3.2.2.

We want now to obtain the phase-space distribution as a function of the density profile ρ, the opposite of what we did in appendix B.1.

We start again from the density as an integral over velocity space, $\rho = \int f\, d^3v$. Now we have an isotropic distribution $f(E)$, i.e. f depends only on the energy, so the volume element in spherical coordinates reduces to $d^3v = 4\pi\, v^2\, dv$. Changing variables through $E = \phi(r) + v^2/2$, the density becomes

$$\rho = 4\pi \int_0^\infty f(E)\, v^2\, dv = 4\pi\sqrt{2} \int_\phi^\infty f(E)\, \sqrt{E-\phi}\, dE, \tag{B.10}$$

where we used $v = \sqrt{2(E-\phi)}$ and $v^2 dv = \sqrt{2}\sqrt{E-\phi}\, dE$.

Since both ρ and ϕ are functions of r, and $\phi(r)$ is monotonic in the region of interest, we can regard ρ as a function of ϕ and differentiate both sides with respect to ϕ

$$\frac{d\rho}{d\phi} = -2\sqrt{2}\,\pi \int_\phi^\infty \frac{f(E)}{\sqrt{E-\phi}}\, dE. \tag{B.11}$$

Equation (B.11) is an Abel integral equation for f.

To invert it, we multiply by $(\phi-\mathcal{E})^{-1/2}$, with $\mathcal{E}$ as a new fixed parameter, and integrate over ϕ from $\mathcal{E}$ to infinity, exchanging the order of integration:

$$\int_{\mathcal{E}}^\infty \frac{d\rho}{d\phi} \frac{d\phi}{\sqrt{\phi-\mathcal{E}}} = -2\sqrt{2}\,\pi \int_{\mathcal{E}}^\infty dE\, f(E) \int_{\mathcal{E}}^E \frac{d\phi}{\sqrt{(\phi-\mathcal{E})(E-\phi)}}. \tag{B.12}$$

The inner integral

$$\int_{\mathcal{E}}^E \frac{d\phi}{\sqrt{(\phi-\mathcal{E})(E-\phi)}} \tag{B.13}$$

is a standard integral, independent of both $\mathcal{E}$ and E, which can be solved explicitly with the substitution $\phi = \mathcal{E} + (E-\mathcal{E})\sin^2\theta$ and becomes

$$2\int_0^{\pi/2} d\theta = \pi. \tag{B.14}$$

Now, substituting this value in eq. (B.12)

$$\int_{\mathcal{E}}^\infty \frac{d\rho}{d\phi} \frac{d\phi}{\sqrt{\phi-\mathcal{E}}} = -2\sqrt{2}\,\pi^2 \int_{\mathcal{E}}^\infty f(E)\, dE, \tag{B.15}$$

and differentiating with respect to $\mathcal{E}$ we obtain Eddington's formula

$$f(E) = \frac{1}{\sqrt{8}\,\pi^2} \frac{d}{dE} \int_E^\infty \frac{d\rho}{d\phi} \frac{d\phi}{\sqrt{\phi-E}}. \tag{B.16}$$

B.4 Radial actions

Here we derive the radial actions used in section 3.2.2.

Power-law potential

For the initial potential

$$\phi(r) = \phi_0 \left(\frac{r}{r_s}\right)^{2-\gamma} \tag{B.17}$$

the action integral cannot be performed in closed form for generic γ, so we will study its scaling with E.

We can obtain the orbit r_E by $\phi(r_E) = E$:

$$r_E = r_s \left(\frac{E}{\phi_0} \right)^{\frac{1}{2-\gamma}} . \tag{B.18}$$

Recalling the radial action expression in eq. (3.5) and rescaling $r = r_E\, x$ we obtain

$$I(E,L) = 2 \int_{r_-}^{r_+} \sqrt{2E - 2\phi(r) - \frac{L^2}{r^2}}\, dr = 2\sqrt{2E}\, r_E \int_{x_-}^{x_+} \sqrt{1 - x^{2-\gamma} - \frac{\lambda^2}{x^2}}\, dx, \tag{B.19}$$

where $\lambda^2 = \frac{L^2}{2E\, r_E^2}$ is dimensionless.

Hence

$$I(E,L) = 2\sqrt{2E}\, r_E\, F(\lambda) \;\propto\; E^{\frac{1}{2}+\frac{1}{2-\gamma}} = E^{\frac{4-\gamma}{2(2-\gamma)}} \tag{B.20}$$

at fixed λ.

Point-mass potential

The final potential is the point-mass

$$\phi'(r) = -\frac{GM_{\rm BH}}{r}, \tag{B.21}$$

so the radial velocity becomes

$$v_r^2 = 2E' + \frac{2GM_{\rm BH}}{r} - \frac{L'^2}{r^2} = \frac{2|E'|}{r^2}\,(r_+ - r)\,(r - r_-)\,, \tag{B.22}$$

where $r_\pm$ are the turning points, with

$$r_+ + r_- = \frac{GM_{\rm BH}}{|E'|}, \qquad r_+ r_- = \frac{L'^2}{2|E'|}. \tag{B.23}$$

The radial action is therefore

$$I' = 2 \int_{r_-}^{r_+} v_r\, dr = 2\sqrt{2|E'|} \int_{r_-}^{r_+} \frac{\sqrt{(r_+ - r)(r - r_-)}}{r}\, dr. \tag{B.24}$$

The definite integral is a standard one and can be evaluated with the substitution $r = r_+ \sin^2\theta + r_- \cos^2\theta$:

$$\int_{r_-}^{r_+} \frac{\sqrt{(r_+ - r)(r - r_-)}}{r}\, dr = \frac{\pi}{2}\,(r_+ + r_-) - \pi\sqrt{r_+ r_-}, \tag{B.25}$$

so that

$$I' = 2\sqrt{2|E'|} \left[\frac{\pi}{2} \frac{GM_{\rm BH}}{|E'|} - \pi \frac{L'}{\sqrt{2|E'|}} \right] = 2\pi \left(-L' + \frac{GM_{\rm BH}}{\sqrt{-2E'}} \right). \tag{B.26}$$

Note that the action vanishes for circular orbits, for which $L' = \frac{GM_{\rm BH}}{\sqrt{-2E'}}$ is the maximum angular momentum at fixed energy.

B.5 Velocity integral for the spike density

Here we perform the velocity integral quoted in section 3.2.2.

We saw that in the region dominated by the black hole the potential is

$$\phi'(r) \simeq -GM_{\rm BH}/r, \tag{B.27}$$

and bound particles have

$$E' = -\frac{GM_{\rm BH}}{r} + \frac{v^2}{2}, \qquad 0 \le v \le v_{\rm esc} = \sqrt{\frac{2GM_{\rm BH}}{r}}. \tag{B.28}$$

The final distribution function, obtained from adiabatic invariance considerations, scales as

$$f'(E') \propto (-E')^{n\frac{2-\gamma}{4-\gamma}}. \tag{B.29}$$

So, the density is given by the integral over velocity space

$$\rho'(r) = 4\pi \int_0^{v_{\rm esc}} f'(E')\, v^2\, dv \;\propto\; \int_0^{v_{\rm esc}} \left(\frac{GM_{\rm BH}}{r} - \frac{v^2}{2}\right)^{n\frac{2-\gamma}{4-\gamma}} v^2\, dv. \tag{B.30}$$

With the substitution $v = v_{\rm esc}\, u$, $u \in [0,1]$, we can factor out all the dependence on r

$$\rho'(r) \;\propto\; \left(\frac{GM_{\rm BH}}{r}\right)^{n\frac{2-\gamma}{4-\gamma}} v_{\rm esc}^3 \int_0^1 \left(1-u^2\right)^{n\frac{2-\gamma}{4-\gamma}} u^2\, du \;\propto\; \left(\frac{GM_{\rm BH}}{r}\right)^{n\frac{2-\gamma}{4-\gamma}+\frac{3}{2}} \;\propto\; r^{-\left(\frac{3}{2}+n\frac{2-\gamma}{4-\gamma}\right)}, \tag{B.31}$$

where the integral in u is a finite constant independent of r, in particular we notice that

$$\int_0^1 \left(1-u^2\right)^{n\frac{2-\gamma}{4-\gamma}} u^2\, du = \frac{1}{2}\int_0^1 t^{1/2}\,(1-t)^{n\frac{2-\gamma}{4-\gamma}}\, dt = \frac{1}{2}\, B\!\left(\frac{3}{2},\; n\,\frac{2-\gamma}{4-\gamma}+1\right), \tag{B.32}$$

where B is Euler's Beta function, whose definition will be better discussed in appendix B.6.

We therefore obtain

$$\rho'(r) \propto r^{-\gamma_{\rm sp}}, \qquad \gamma_{\rm sp} = \frac{3}{2} + n\,\frac{2-\gamma}{4-\gamma}. \tag{B.33}$$

B.6 Distribution function of the power-law halo

Here we derive the Gondolo–Silk distribution function used in section 3.2.3.

For the power law halo

$$\rho(r) = \rho_s \left(\frac{r}{r_s}\right)^{-\gamma}, \qquad 0 < \gamma < 2, \tag{B.34}$$

it is possible to evaluate Eddington's formula exactly.

We recall Eddington's formula of eq. (B.16)

$$f(E) = \frac{1}{\sqrt{8}\,\pi^2} \frac{d}{dE} \int_E^\infty \frac{d\rho}{d\phi} \frac{d\phi}{\sqrt{\phi - E}}, \tag{B.35}$$

and the potential of eq. (B.9), which is exact for the considered density profile,

$$\phi(r) = \frac{4\pi G\rho_s r_s^\gamma}{3-\gamma}\int_0^r r'^{\,1-\gamma}\, dr' = \phi_0 \left(\frac{r}{r_s}\right)^{2-\gamma}, \qquad \phi_0 = \frac{4\pi G\rho_s r_s^2}{(3-\gamma)(2-\gamma)}. \tag{B.36}$$

Combining eq. (B.34) with eq. (B.36) we can eliminate the radius

$$\rho(\phi) = \rho_s \left(\frac{\phi}{\phi_0}\right)^{-p}, \qquad p \equiv \frac{\gamma}{2-\gamma}, \qquad \frac{d\rho}{d\phi} = -\frac{p\,\rho_s}{\phi_0}\left(\frac{\phi}{\phi_0}\right)^{-p-1}. \tag{B.37}$$

Now the integral in eq. (B.35) can be computed with the substitution $\phi = E/x$, $x \in (0,1]$:

$$\int_E^\infty \phi^{-p-1}\,(\phi - E)^{-1/2}\, d\phi = E^{-p-1/2}\int_0^1 x^{\,p-1/2}(1-x)^{-1/2}\, dx = E^{-p-1/2}\, B\big(p+\tfrac{1}{2}, \tfrac{1}{2}\big)\,, \tag{B.38}$$

where B is Euler's Beta function, defined for $a, b > 0$ as

$$B(a,b) = \int_0^1 x^{\,a-1}(1-x)^{\,b-1}\, dx = \frac{\Gamma(a)\,\Gamma(b)}{\Gamma(a+b)}, \tag{B.39}$$

with Γ Euler's Gamma function,

$$\Gamma(z) = \int_0^\infty t^{\,z-1} e^{-t}\, dt, \qquad z > 0. \tag{B.40}$$

The convergence of the integral in eq. (B.38) is guaranteed because $p + \frac{1}{2} > 0$, since $p = \frac{\gamma}{2-\gamma} > 0$ for $0 < \gamma < 2$.

Taking the derivative with respect to E, we obtain

$$f(E) = \frac{\rho_s\,\phi_0^p}{\sqrt{8}\,\pi^2}\, p\,\big(p+\tfrac{1}{2}\big)\, B\big(p+\tfrac{1}{2}, \tfrac{1}{2}\big)\, E^{-p-3/2}, \tag{B.41}$$

so that $f(E) \propto E^{-n}$ with

$$n = p + \frac{3}{2} = \frac{6-\gamma}{2(2-\gamma)}. \tag{B.42}$$

The coefficient can be simplified using the properties of Euler's Beta and Gamma functions:

$$\Gamma(z+1) = z\,\Gamma(z), \qquad \Gamma\big(\tfrac{1}{2}\big) = \sqrt{\pi}, \tag{B.43}$$

and in our particular case

$$B\big(p+\tfrac{1}{2}, \tfrac{1}{2}\big) = \sqrt{\pi}\,\frac{\Gamma\big(p+\tfrac{1}{2}\big)}{\Gamma(p+1)}, \tag{B.44}$$

together with the identities

$$\big(p+\tfrac{1}{2}\big)\,\Gamma\big(p+\tfrac{1}{2}\big) = \Gamma\big(p+\tfrac{3}{2}\big) = \Gamma(n), \qquad \frac{p}{\Gamma(p+1)} = \frac{1}{\Gamma(p)} = \frac{1}{\Gamma\big(n-\tfrac{3}{2}\big)}. \tag{B.45}$$

Finally we obtain the Gondolo–Silk distribution function

$$f(E) = \frac{\rho_s}{(2\pi\phi_0)^{3/2}}\,\frac{\Gamma(n)}{\Gamma\big(n-\tfrac{3}{2}\big)}\left(\frac{\phi_0}{E}\right)^n. \tag{B.46}$$

B.7 Scaling of the singular terms in Eddington's formula

Here we derive the scaling used in section 3.2.4.

We recall the expansion of Eddington's integral of eq. (3.35)

$$f(E) \sim \int_{r_\star}^{R} \frac{dr}{r^3} \frac{c_0 + c_1(r/r_s)^\alpha + c_2(r/r_s)^{2\alpha} + \dots}{\sqrt{r^{2-\gamma} - E}}, \tag{B.47}$$

where the lower limit $r_\star = E^{1/(2-\gamma)}$ is the radius at which $\phi(r_\star) = E$, while R is an arbitrary upper radius, of the order of the scale radius of the halo. We set $\phi_0 = r_s = 1$, since we are only interested in the scaling with E.

A term $\propto r^k$ in the numerator gives the contribution

$$I_k(E) = \int_{r_\star}^{R} \frac{r^{\,k-3}}{\sqrt{r^{2-\gamma} - E}}\, dr. \tag{B.48}$$

Rescaling $r = r_\star x$ and using $r_\star^{2-\gamma} = E$, so that $r^{2-\gamma} - E = E\,(x^{2-\gamma} - 1)$, we obtain

$$I_k(E) = r_\star^{\,k-2}\, E^{-1/2} \int_{1}^{R/r_\star} \frac{x^{\,k-3}\, dx}{\sqrt{x^{2-\gamma} - 1}} \;\propto\; E^{\frac{k-2}{2-\gamma} - \frac{1}{2}} = E^{-n_k}, \qquad n_k = \frac{6 - \gamma - 2k}{2(2-\gamma)}, \tag{B.49}$$

then the scaling is all in the prefactor, provided that the dimensionless integral in x tends to a finite constant as $E \to 0^+$. We therefore examine its two endpoints.

At the lower endpoint the integrand is singular, but integrably, so expanding $x^{2-\gamma} - 1 \simeq (2-\gamma)(x-1)$ for $x \to 1^+$, it behaves as $(x-1)^{-1/2}$ and never produces a divergence of $f(E)$.

At the upper endpoint, where $E \to 0^+$ implies $R/r_\star \to \infty$, the integrand behaves as $x^{\,k-3-(2-\gamma)/2}$, so the integral converges if and only if

$$k - 3 - \frac{2-\gamma}{2} < -1 \quad \Longleftrightarrow \quad n_k > 0, \tag{B.50}$$

i.e. the condition of convergence at large x is precisely the condition that the exponent n_k be positive. Instead, when $n_k \leq 0$, the integral is dominated by large radii and I_k contributes only to the regular part of $f(E)$, as discussed in section 3.2.4.

For $k = 0$ one recovers $n_0 = \frac{6-\gamma}{2(2-\gamma)}$, in agreement with the exact result of Gondolo and Silk. For a cored profile, with $\gamma = 0$ and $k = \alpha$, one obtains $n_\alpha = \frac{3-\alpha}{2}$, which is the case analysed in Ref. [42]. For the non-singular isothermal profile, with $\gamma = 0$ and $\alpha = 2$, both c_0 and c_1 vanish and the first surviving term has $k = 2\alpha = 4$, for which $n_4 = -1/2 < 0$: no term of the expansion produces a divergence, hence $f(E)$ is regular and $n = 0$.

Appendix C

Saturation density from dark matter annihilation

In this appendix we derive the saturation density of section 3.2.5.

The density growth in the innermost region of the DM spike is depleted because DM annihilates efficiently on account of very high DM density. The evolution of the density due to annihilation is

$$\frac{\partial \rho}{\partial t} = -\frac{\langle \sigma v \rangle}{m_{\mathrm{DM}}}\, \rho^2, \tag{C.1}$$

where m_{DM} is the DM mass and $\langle \sigma v \rangle$ is the cross section.

Equation (C.1) is a separable first-order differential equation, so writing it as

$$\frac{d\rho}{\rho^2} = -\frac{\langle \sigma v \rangle}{m_{\mathrm{DM}}}\, dt, \tag{C.2}$$

and integrating from the initial density ρ_i at the time of black hole formation up to the density ρ at a later time t

$$\int_{\rho_i}^{\rho} \frac{d\rho'}{\rho'^2} = -\frac{\langle \sigma v \rangle}{m_{\mathrm{DM}}} \int_0^t dt', \tag{C.3}$$

we obtain

$$\frac{1}{\rho} = \frac{1}{\rho_i} + \frac{\langle \sigma v \rangle}{m_{\mathrm{DM}}}\, t. \tag{C.4}$$

Considering a very large initial density we can neglect the term $1/\rho_i$ and the equation becomes

$$\rho(t) \simeq \frac{m_{\mathrm{DM}}}{\langle \sigma v \rangle\, t}. \tag{C.5}$$

Finally, we obtain the saturation density evaluating eq. (C.5) at the age of the black hole $t = t_{\mathrm{BH}}$, conservatively 10^{10} yr, the maximum time over which annihilation has been acting,

$$\rho_{\mathrm{core}} = \frac{m_{\mathrm{DM}}}{\langle \sigma v \rangle\, t_{\mathrm{BH}}}. \tag{C.6}$$

ρ_{core} can be obtained also as the density at which the characteristic annihilation timescale $t_{\mathrm{ann}} \sim m_{\mathrm{DM}}/(\langle \sigma v \rangle\, \rho)$ becomes comparable to t_{BH}.

Bibliography

[1] M. Cirelli et al. *Dark Matter*, 2025[2406.01705].

[2] H.E.S.S. Collaboration, *Search for Dark Matter Annihilation Signals in the H.E.S.S. Inner Galaxy Survey*, Physical Review Letters 129 (2022), 111101[2207.10471].

[3] Planck Collaboration, *Planck 2018 results. VI. Cosmological parameters*, Astronomy & Astrophysics 641 (2020), A6[1807.06209].

[4] S. Profumo, *TASI 2012 Lectures on Astrophysical Probes of Dark Matter*, 2013[1301.0952].

[5] G. Arcadi et al. *The waning of the WIMP: endgame?*, The European Physical Journal C 85 (2025), 2[2403.15860].

[6] L. Bergström, *Non-baryonic dark matter: observational evidence and detection methods*, Reports on Progress in Physics 63 (2000), 793–841[hep-ph/0002126].

[7] G. Jungman et al. *Supersymmetric dark matter*, Physics Reports 267 (1996), 195–373[hep-ph/9506380].

[8] V. C. Rubin and W. K. Ford Jr., *Rotation of the Andromeda Nebula from a Spectroscopic Survey of Emission Regions*, The Astrophysical Journal 159 (1970), 379.

[9] J. F. Navarro et al. *The Structure of Cold Dark Matter Halos*, The Astrophysical Journal 462 (1996), 563–575[astro-ph/9508025].

[10] J. F. Navarro et al. *A Universal Density Profile from Hierarchical Clustering*, The Astrophysical Journal 490 (1997), 493–508[astro-ph/9611107].

[11] M. Lisanti, *The Physics of Dark Matter*, ICTP Trieste, 2018.

[12] F. Zwicky, *Die Rotverschiebung von extragalaktischen Nebeln*, Helvetica Physica Acta 6 (1933), English translation: *Gen. Rel. Grav.* **41** (2009) 207, 10.1007/s10714-008-0707-4, 110–127.

[13] H. Andernach and F. Zwicky, *English and Spanish Translation of Zwicky's (1933) The Redshift of Extragalactic Nebulae*, 2017[1711.01693].

[14] G. Bertone and D. Hooper, *History of dark matter*, Rev. Mod. Phys. 90 (2018), 045002[1605.04909].

[15] M. Colless and A. M. Dunn, *Structure and Dynamics of the Coma Cluster*, The Astrophysical Journal 458 (1996), 435[astro-ph/9508070].

[16] D. Clowe et al. *A Direct Empirical Proof of the Existence of Dark Matter*, The Astrophysical Journal 648 (2006), L109–L113[astro-ph/0608407].

[17] M. Milgrom, *A modification of the Newtonian dynamics as a possible alternative to the hidden mass hypothesis*, The Astrophysical Journal 270 (1983), 365–370.

[18] M. Milgrom, *A modification of the Newtonian dynamics: Implications for galaxies*, The Astrophysical Journal 270 (1983), 371–383.

[19] M. Milgrom, *A modification of the Newtonian dynamics: Implications for galaxy systems*, The Astrophysical Journal 270 (1983), 384–389.

[20] R. Scarpa, *Modified Newtonian Dynamics, an Introductory Review*, AIP Conference Proceedings, vol. 822, AIP, 2006, 253–265[astro-ph/0601478].

[21] K. G. Begeman et al. *Extended rotation curves of spiral galaxies: dark haloes and modified dynamics*, Mon. Not. R. Astron. Soc. 249 (1991), 523–537.

[22] J. Bekenstein and M. Milgrom, *Does the missing mass problem signal the breakdown of Newtonian gravity?*, The Astrophysical Journal 286 (1984), 7–14.

[23] T. R. Slatyer, *TASI Lectures on Indirect Detection of Dark Matter*, 2017[1710.05137].

[24] D. Hooper, *TASI lectures on indirect searches for dark matter*, 2018[1812.02029].

[25] B. Moore et al. *Cold Collapse and the Core Catastrophe*, Monthly Notices of the Royal Astronomical Society 310 (1999), 1147–1152[astro-ph/9903164].

[26] J. Einasto, *On the Construction of a Composite Model for the Galaxy and on the Determination of the System of Galactic Parameters*, 1965.

[27] K. G. Begeman et al. *Extended Rotation Curves of Spiral Galaxies: Dark Haloes and Modified Dynamics*, Monthly Notices of the Royal Astronomical Society 249 (1991), 523–537.

[28] A. Burkert, *The Structure of Dark Matter Halos in Dwarf Galaxies*, The Astrophysical Journal Letters 447 (1995), L25–L28[astro-ph/9504041].

[29] M. Cirelli et al. *PPPC 4 DM ID: a poor particle physicist cookbook for dark matter indirect detection*, Journal of Cosmology and Astroparticle Physics 2011 (2011), 051[1012.4515].

[30] J. I. Read, *The local dark matter density*, Journal of Physics G: Nuclear and Particle Physics 41 (2014), 063101[1404.1938].

[31] V. Lefranc et al. *Dark Matter in γ lines: Galactic Center vs. dwarf galaxies*, Journal of Cosmology and Astroparticle Physics 2016 (2016), 043[1608.00786].

[32] G. Steigman et al. *Precise relic WIMP abundance and its impact on searches for dark matter annihilation*, Physical Review D 86 (2012), 023506[1204.3622].

[33] J. A. Hinton, *The status of the H.E.S.S. project*, New Astronomy Reviews 48 (2004), 331–337[astro-ph/0403052].

[34] F. Aharonian et al. *Observations of the Crab nebula with HESS*, Astronomy & Astrophysics 457 (2006), 899–915[astro-ph/0607333].

[35] A. Eckart and R. Genzel, *Stellar proper motions in the central 0.1 pc of the Galaxy*, Monthly Notices of the Royal Astronomical Society 284 (1997), 576–598.

[36] A. M. Ghez et al. *High Proper-Motion Stars in the Vicinity of Sagittarius A*: Evidence for a Supermassive Black Hole at the Center of Our Galaxy*, The Astrophysical Journal 509 (1998), 678–686[astro-ph/9807210].

[37] A. M. Ghez et al. *Measuring Distance and Properties of the Milky Way's Central Supermassive Black Hole with Stellar Orbits*, The Astrophysical Journal 689 (2008), 1044–1062[0808.2870].

[38] S. Gillessen et al. *Monitoring Stellar Orbits around the Massive Black Hole in the Galactic Center*, The Astrophysical Journal 692 (2009), 1075–1109[0810.4674].

[39] GRAVITY Collaboration, *A geometric distance measurement to the Galactic center black hole with 0.3% uncertainty*, Astronomy & Astrophysics 625 (2019), L10[1904.05721].

[40] P. Gondolo and J. Silk, *Dark Matter Annihilation at the Galactic Center*, Physical Review Letters 83 (1999), 1719–1722[astro-ph/9906391].

[41] J. Binney and S. Tremaine, *Galactic Dynamics*, 2nd ed., Princeton Series in Astrophysics, Princeton, NJ: Princeton University Press, 2008, ISBN: 978-0-691-13026-2.

[42] P. Ullio et al. *Dark-matter spike at the galactic center?*, Physical Review D 64 (2001), 043504[astro-ph/0101481].

[43] H. Zhao, *Analytical models for galactic nuclei*, Monthly Notices of the Royal Astronomical Society 278 (1996), 488–496[astro-ph/9509122].

[44] G. D. Quinlan et al. *Models of Galaxies with Central Black Holes: Adiabatic Growth in Spherical Galaxies*, The Astrophysical Journal 440 (1995), 554[astro-ph/9407005].

[45] L. Sadeghian et al. *Dark matter distributions around massive black holes: A general relativistic analysis*, Physical Review D 88 (2013), 063522[1305.2619].

[46] S. L. Shapiro and J. Shelton, *Weak annihilation cusp inside the dark matter spike about a black hole*, Physical Review D 93 (2016), 123510[1606.01248].

[47] GRAVITY Collaboration, R. Abuter, et al. *Mass distribution in the Galactic Center based on interferometric astrometry of multiple stellar orbits*, Astronomy & Astrophysics 657 (2022), L12[2112.07478].

[48] G. Heißel et al. *The dark mass signature in the orbit of S2*, Astronomy & Astrophysics 660 (2022), A13[2112.07778].

[49] M. Habibi et al. *Spectroscopic Detection of a Cusp of Late-type Stars around the Central Black Hole in the Milky Way*, The Astrophysical Journal Letters 872 (2019), L15[1902.07219].

[50] R. Pechetti et al. *Luminosity models and density profiles for nuclear star clusters for a nearby volume-limited sample of 29 galaxies*, The Astrophysical Journal 900 (2020), 32[1911.09686].

[51] E. Gallego-Cano et al. *New constraints on the structure of the nuclear stellar cluster of the Milky Way from star counts and MIR imaging*, Astronomy & Astrophysics 634 (2020), A71[2001.08182].

[52] S. L. Shapiro and D. C. Heggie, *Effect of stars on the dark matter spike around a black hole: A tale of two treatments*, Physical Review D 106 (2022), 043018[2209.08105].

[53] S. Balaji et al. *Dark Matter spikes around Sgr A* in γ-rays*, 2023[2303.12107].

[54] O. Sameie et al. *The central densities of Milky Way-mass galaxies in cold and self-interacting dark matter models*, Monthly Notices of the Royal Astronomical Society 507 (2021), 720–729[2102.12480].

[55] D. Merritt, *Evolution of the Dark Matter Distribution at the Galactic Center*, Physical Review Letters 92 (2004), 201304[astro-ph/0311594].

[56] O. Y. Gnedin and J. R. Primack, *Dark Matter Profile in the Galactic Center*, Physical Review Letters 93 (2004), 061302[astro-ph/0308385].

[57] V. Belokurov et al. *Co-formation of the disc and the stellar halo*, Monthly Notices of the Royal Astronomical Society 478 (2018), 611–619[1802.03414].

[58] A. Helmi et al. *The merger that led to the formation of the Milky Way's inner stellar halo and thick disk*, Nature 563 (2018), 85–88[1806.06038].

[59] I. Ciucă et al. *Chasing the impact of the Gaia-Sausage-Enceladus merger on the formation of the Milky Way thick disc*, Monthly Notices of the Royal Astronomical Society: Letters 528 (2024), L122–L126[2211.01006].

[60] H.E.S.S. Collaboration, *Acceleration of petaelectronvolt protons in the Galactic Centre*, Nature 531 (2016), 476–479[1603.07730].

[61] Y. Gouttenoire and F. Sala, *BSM in the Sky, Exercises for the Summer School on BSM Particle Physics and Cosmology, Ljubljana*, 2019.